THE ASTROPHYSICAL JOURNAL, 299:167–190, 1985 December 1

A PERIODIC SHOCK WAVE MODEL FOR MIRA VARIABLE ATMOSPHERES

EDMUND BERTSCHINGER AND ROGER A. CHEVALIER
Department of Astronomy, University of Virginia
Received 1985 January 28; accepted 1985 May 20

ABSTRACT

We have derived a semianalytic model for the time-dependent structure of a stellar atmosphere traversed by periodic shock waves. The derivation assumes that (1) motions are purely periodic (no mass loss); (2) the shock waves are radiative, with postshock cooling time much less than the period; and (3) the postshock motion of individual fluid elements is adiabatic, with arbitrary adiabatic exponent and entropy distribution. An analytic solution is first presented for a plane-parallel atmosphere. This solution underlies an approximate solution to the more general spherical problem.

The model is applied to Mira variables. Observations by Hinkle and coworkers of the CO $\Delta v = 3$ vibration-rotation bands in four Mira variables (o Cet, T Cep, χ Cyg, and R Cas) have been analyzed and show a good fit to the model, enabling us to determine the radius, shock strength, and density in the layer where the lines form. The derived pulsation constants do not resolve the dispute over pulsation mode because of the uncertainty in stellar masses. The shock model implies that very large (up to $\sim 10^4\ L_\odot$) shock luminosities exist during premaximum phases. Rough estimates of mass loss based on the breakdown of radiative cooling at low densities and the formation and radiative acceleration of dust grains lead to rates up to $\sim 10^{-6}\ M_\odot\ \mathrm{yr}^{-1}$; the latter mechanism is probably necessary to produce terminal velocities as high as are observed.

Subject headings: shock waves — stars: long-period variables — stars: pulsation

I. INTRODUCTION

Long-period (or Mira) variables present a number of enigmas that have made understanding their atmospheric structure difficult. They typically vary by 5 or more visual magnitudes during a period of about 1 year, but their bolometric luminosity, most of it in the infrared, changes much less. They show strong Balmer and fluorescence emission lines at phases near visual maximum (Merrill 1947), but the visual absorption lines show little velocity variation (Joy 1954). They are surrounded by large dusty envelopes, often with SiO (Snyder and Buhl 1975; Clark *et al.* 1981) and OH (Reid 1976) masers. They typically have mass loss rates of $\sim 10^{-6}\ M_\odot\ \mathrm{yr}^{-1}$ (Gehrz and Woolf 1971; Bowers and Kerr 1977; Knapp and Morris 1984). The interpretation of these disparate observations is that shock waves propagate through Mira atmospheres once a period, producing the emission lines and aiding the mass loss process. The atmospheres are very opaque in the visual, so the absorption lines are thought to form in a circumstellar shell, perhaps near the SiO masers (Hinkle, Hall, and Ridgway 1982).

Early shock wave models of Gorbatskii (1961) and Tsuji (1971) sought mainly to explain the optical (and near-infrared) emission- and absorption-line observations. The task of constructing model Mira atmospheres eased considerably when infrared observations probing deeper layers became available (Maehara 1971; Hinkle 1978; Hinkle and Barnes 1979*a*, *b*). These new data guided Wood (1979) and Willson and Hill (1979) in presenting fairly detailed calculations of the atmospheric motions and helped them to draw tentative conclusions about the size and mode of pulsation of Mira variables and the cause of their high mass loss rates. Unfortunately, the conclusions of these two groups were often contradictory (Willson 1982; Wood 1982).

Recent advances in high-resolution infrared spectroscopy provide a new opportunity for understanding shock waves in Mira variables. Hinkle and his coworkers (Hinkle, Hall, and Ridgway 1982; Hinkle, Scharlach, and Hall 1984) have obtained radial velocities, excitation temperatures, and CO column densities for vibration-rotation transitions in the 2 μm spectral region. These observations provide a wealth of data that would be difficult to assimilate in earlier shock models, spurring us to develop a more realistic model. The model is semianalytic rather than numerical, with the consequent advantage that we do not have to worry about numerical techniques affecting our results in unknown ways; our model thus provides a computational test for numerical models.

To derive the shock model, we assume that (1) the atmospheric motions are purely periodic, so that fluid elements return to their initial conditions after one period; (2) the shock waves are radiative, i.e., shocked gas quickly cools by emission of radiation in a thin layer behind the shock front; and (3) the postshock motion of individual fluid elements is adiabatic, but with arbitrary exponent (= ratio of specific heats) and specific entropy. Assumptions 1 and 2 are perfectly correct sufficiently deep in the atmosphere, while assumption 3 is an *Ansatz* that allows us to obtain a semianalytic solution. By "adiabaticity" we mean that the postshock fluid elements evolve with a fixed ratio of specific heats γ, i.e., $d \ln p / d \ln \rho = \gamma$ is a constant for a fixed fluid element. Since γ is arbitrary and may vary with Lagrangian coordinate (in the spherical case), assumption 3 is more general than the isothermal or adiabatic assumptions made by Hill and Willson (1979) and Wood (1979).

In § II we present the shock solution in the plane-parallel limit where fluid elements move distances that are small compared with the stellar radius. In this case an analytic solution can be found. Unfortunately, it is easy to demonstrate that the plane-parallel assumption is violated for long-period (and other) variables. In § III we therefore generalize the solution to allow certain quantities to vary with radius. An exact analytic solution is then no longer possible, but we obtain an approx-

imate semianalytic solution by dividing Lagrangian fluid trajectories into "planar" and "spherical" parts. The variation of the adiabatic exponent and specific entropy with radius are left arbitrary, to be specified by observations or some assumption about the thermodynamic properties of the atmosphere. The model is hydrodynamic only; we do not treat radiative transfer or the effect of the radiation on the gas.

In § IV we fit our model atmospheres to the best data presently available, the CO $\Delta v = 3$ vibration-rotation band observations of Hinkle, Hall, and Ridgway (1982) and Hinkle, Scharlach, and Hall (1984). The thermodynamic quantities and radius are obtained from fits to the phase-dependent excitation temperatures and velocities; from these and the column densities we obtain a complete hydrodynamic description of the region in which the lines form. By making an assumption about the thermodynamic properties of gas at other heights, we are able to extrapolate the model to describe a large range in radius. In this way we calculate a model shock luminosity curve, and conclude that at early phases the visual luminosity of Mira variables is dominated by shock emission.

In § V*a* we try applying the model results to the question of what pulsation mode is appropriate for Mira variables. Unfortunately the result depends importantly on the stellar masses, which are not known well enough to answer the question. We have better success adddressing mass loss (§ V*b*). We show that radiation pressure on grains condensing in the cool layers pushed up by the shocks is the most likely source of mass loss. We conclude (§ V*c*) with several suggestions of how the results of this paper may be extended to obtain a still better understanding of Mira variable atmospheres.

II. PLANE-PARALLEL PERIODIC SHOCKS

In this section we derive an analytic solution for the structure of a plane-parallel, pulsating stellar atmosphere traversed by periodic shocks. We will find that the plane-parallel assumption is violated for long period variables, but it lays the foundation for a more general approximate spherical treatment.

Figure 1 is a schematic diagram of the atmospheric structure between two shocks. In the plane-parallel limit considered here, an infinite series of shocks coexists in the atmosphere, but determining the structure between two shocks is sufficient to give the structure everywhere. The upper shock is at a height $z = z_s(t)$. The preshock gas enters the shock with speed u_1 (measured in the shock frame), density ρ_1, and pressure $p_1 = \rho_1 u_1^2/(\gamma \mathcal{M}_1^2)$, where $\mathcal{M}_1$ is the preshock Mach number and γ is the effective adiabatic exponent (ratio of specific heats) of the gas. The shocked gas radiatively cools to a temperature T_c in a thin layer behind the shock. If $u_1 \gtrsim 60$ km s^{-1}, the shock may be preceded by a radiative precursor (Shull and McKee 1979; Gillet and Lafon 1983, 1984), where molecules are photodissociated and H is photoionized by Lyman continuum radiation emitted behind the shock. We are not concerned here with the structure of the cooling layer or precursor, provided that they are thin compared with other dimensions. This will be the case in the lower atmosphere, but at high altitudes cooling will become ineffective, and the model will break down (§ V*b*).

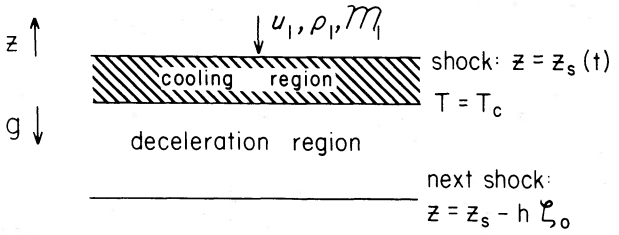

FIG. 1.—Schematic view of the atmospheric structure between two shock waves in a Mira variable. Gas enters the upper shock with density ρ_1 and velocity u_1 (in the shock frame); the Mach number is $\mathcal{M}_1$. The gas cools to a temperature T_c by emission of radiation in a thin cooling layer, below which the gas is decelerated by gravity before being shocked again. (The relative thickness of the cooling layer is greatly exaggerated here.) Many shocks may be present, with a new one forming at the base of the atmosphere every period.

We assume here that T_c—which is determined by atomic physics—is independent of shock height; that after the gas relaxes it has the same chemical state as the preshock gas (i.e., the same mean molecular weight μ and effective adiabatic exponent γ); and that this chemical state is independent of height. The chemical state differs in the cooling region because of dissociation, ionization, and recombination, but the details of these processes may be ignored here, since we are concerned only with the state of the gas after it has relaxed. The motion of individual fluid elements is treated after cooling as being effectively adiabatic with exponent γ, but the specific entropy may vary from element to element. We do not assume that the atmosphere is isothermal unless $\gamma = 1$; our derivation holds for any $\gamma \geq 1$. In the spherical generalization of the periodic shock solution (§ III), T_c, μ, and γ are allowed to vary with height, as they do in a real star. We neglect their variation here, however, in the spirit of the plane-parallel approximation.

After the gas cools radiatively, it passes through a deceleration region, where gravitational forces are important. (Gravity may be neglected in the cooling region, where time scales are much less than one period.) A gas element is initially accelerated upward by the shock, then gradually decelerates and falls back to its original height before being shocked again. We assume strict periodicity with zero mass loss, so that a fixed fluid element is always shocked at the same height. We will show later that this assumption is valid in the dense lower part of the atmosphere even if there is mass loss occurring from higher altitudes.

Because of the plane-parallel assumption, the gravitational deceleration $g = GM/R^2$ is constant. The isothermal cooling sound speed $C_c \equiv (kT_c/\mu)^{1/2}$ is also constant by assumption. Since strict periodicity also requires that the period P ($\equiv$ the time interval between successive shock passages through a fixed gas element) be a constant independent of height, it follows from dimensional analysis that u_1 is independent of shock height. (The period is constant and must be proportional to both C_c/g and u_1/g.) If u_1 is constant, the shock velocity v_s (measured in the stellar rest frame) is also constant. Observations of Mira variables indicate that u_1 actually varies with height (Fox, Wood, and Dopita 1984), so the plane-parallel and constant cooling sound speed assumptions cannot both be fully valid. In § III we will relax these assumptions, with the results (§ IV) showing a good fit to the observations.

We now solve for the fluid motion in the deceleration region. The fluid equations are

$$\frac{d\rho}{dt} \equiv \left(\frac{\partial}{\partial t} + v\frac{\partial}{\partial z}\right)\rho = -\rho(\nabla \cdot \boldsymbol{v})\,, \tag{2.1}$$

$$\frac{dv}{dt} + \frac{1}{\rho}\frac{\partial p}{\partial z} = -g\,, \tag{2.2}$$

$$\frac{dp}{dt} + \gamma p(\nabla \cdot \boldsymbol{v}) = 0\,. \tag{2.3}$$

These are respectively the continuity, Euler, and energy equations. The velocity $\boldsymbol{v} = v\boldsymbol{e}_z$ is in the vertical direction, and is measured in the stellar rest frame. In the plane-parallel limit $\nabla \cdot \boldsymbol{v} = \partial v/\partial z$; more generally, $\nabla \cdot \boldsymbol{v} = \partial v/\partial r + 2v/r$, where r is the radius measured from the center of the star. Note that the heat equation can always be written in the form of equation (2.3) (with γ varying in general with position and time), but we make the simplifying assumption that γ is a constant.

The exact form of the energy equation is (e.g., Goldreich and Scoville 1976)

$$\frac{d\epsilon}{dt} = \frac{p}{\rho^2}\frac{d\rho}{dt} - \frac{(C - H)}{m_{H_2} n_{H_2}(1 + f/2)}, \tag{2.4}$$

where ϵ is the internal energy per gram including dissociation energy, C is the rate of radiative cooling (in ergs cm^{-3} s^{-1}), H is the rate of radiative heating, m_{H_2} is the mass of a hydrogen molecule, n_{H_2} is the density of molecular hydrogen, and f is the ratio of atomic to molecular hydrogen. The internal energy is related to the density and temperature through the equation of state. Here the thermodynamics of the gas and the interaction of the gas with radiation are described by an effective adiabatic exponent γ. We infer effective values of γ from observations of Mira variables (§ IV) and then discuss the physical basis for γ.

It is convenient to nondimensionalize the fluid variables in terms of u_1, ρ_1, and g. We first define the scale height

$$h \equiv u_1^2/g . \tag{2.5}$$

The fluid variables are now written

$$t = h\tau/u_1 , \quad z = v_s t - h\zeta \equiv h(\delta\tau - \zeta) ,$$
$$v = u_1 V = v_s - u_1 U = u_1(\delta - U) , \quad \rho = \rho_1(z_s) D ,$$
$$p = \rho_1(z_s) u_1^2 P , \quad T = \frac{\mu u_1^2}{k}\theta . \tag{2.6}$$

Here ζ is the distance behind the shock in units of h; U is the downward velocity as seen in the shock frame in units of u_1; and so on. The ideal gas law gives $\theta = P/D$. (The dimensionless pressure P should not be confused with the period; the difference will be clear from the context.) Note that u_1, $v_s = \delta u_1$, and h are constants, but the preshock density generally varies with the shock height z_s. Nondimensionalizing the fluid equations (2.1)–(2.3) now yields

$$\frac{\partial D}{\partial \tau} + \frac{\partial}{\partial \zeta}(DU) = -\delta h \frac{d \ln \rho_1}{dz_s} D , \tag{2.7}$$

$$\frac{\partial U}{\partial \tau} + U\frac{\partial U}{\partial \zeta} + \frac{1}{D}\frac{\partial P}{\partial \zeta} = 1 , \tag{2.8}$$

$$\frac{\partial P}{\partial \tau} + U\frac{\partial P}{\partial \zeta} + \gamma P \frac{\partial U}{\partial \zeta} = -\delta h \frac{d \ln \rho_1}{dz_s} P . \tag{2.9}$$

Boundary conditions for the fluid variables are applied above the shock, immediately below the cooling layer, and at the base of the deceleration region. First, from equations (2.6), at $z = z_s^+, \zeta = 0^-$,

$$U = U_1 \equiv 1 , \quad D = D_1 \equiv 1 , \quad P = \theta = \theta_1 \equiv (\gamma \mathcal{M}_1^2)^{-1} . \tag{2.10}$$

Next, provided that the cooling layer is thin ($u_1 t_{cool} \ll h$), mass and momentum fluxes are constant throughout the cooling region, so, while the gas cools, we have

$$DU = D_1 U_1 = 1 ,$$
$$P + DU^2 = P_1 + D_1 U_1^2 = 1 + \theta_1 . \tag{2.11}$$

At the top of the deceleration region the gas has cooled to $T_c \equiv (\mu u_1^2/k)\theta_c$, giving, for $\zeta = 0^+$,

$$D = D_c , \quad U = D_c^{-1} , \quad P = \theta_c D_c , \tag{2.12}$$

where D_c follows from θ_1 and θ_c: D_c is the larger root of

$$\theta_c D_c^2 - (1 + \theta_1)D_c + 1 = 0 . \tag{2.13}$$

At the base of the deceleration region, $\zeta \equiv \zeta_0$, periodicity implies that the solution must match the preshock boundary conditions for the next shock,

$$U = 1 , \quad D = \frac{\rho_1(z_s - h\zeta_0)}{\rho_1(z_s)} , \quad P = D\theta_1 , \quad \theta = \theta_1 . \tag{2.14}$$

Note that in the shock frame the flow is subsonic at $\zeta = 0$, with Mach number squared $\mathcal{M}^2 \equiv \rho(v - v_s)^2/(\gamma p) = 1/(\gamma\theta_c D_c^2) < 1$, but is supersonic at $\zeta = \zeta_0$: $\mathcal{M}^2 = \mathcal{M}_1^2 > 1$. The flow must therefore contain a sonic point in the deceleration region, where $\mathcal{M} = 1$.

For the flow to be periodic, since the nondimensional preshock density $D_1 = 1$ is a constant, the nondimensional density in front of the next shock must also be a constant, and can be written $D(\tau, \zeta_0) = \exp(\alpha\zeta_0)$, for some constant α. It follows that $d \ln \rho_1/dz_s = -\alpha/h$ is a constant, giving

$$\rho_1(z_s) = \rho_0 e^{-\alpha z_s/h} , \tag{2.15}$$

where ρ_0 is the preshock density at the fiducial height $z_s = 0$. Now the boundary conditions at $\zeta = 0$ and $\zeta = \zeta_0$ for the fluid equations (2.7)–(2.9) are all steady (independent of τ), so the nondimensional solution must also be steady, giving $\partial/\partial\tau = 0$, $\partial/\partial\zeta \rightarrow d/d\zeta$. Note that at a fixed time, the preshock density distribution is not exponential (since other shocks occur higher in the atmosphere), but as a given shock propagates upward, the density immediately in front of it falls off exponentially with time (with density scale height h/α).

To solve the nondimensional fluid equations, we write them in the form

$$\frac{dU}{d\zeta} = \frac{U - \alpha\delta\theta}{U^2 - \gamma\theta} , \tag{2.16}$$

$$U\frac{d}{d\zeta}\ln(DU) = \alpha\delta , \tag{2.17}$$

$$\frac{d}{d\zeta}\ln\theta = -(\gamma - 1)\frac{d}{d\zeta}\ln U . \tag{2.18}$$

Equation (2.18) may be integrated at once to give

$$\theta = \theta_1 U^{-(\gamma - 1)} , \tag{2.19}$$

since $U = 1$, $\theta = \theta_1$ at $\zeta = \zeta_0$. Equation (2.19) must hold also at $\zeta = 0$, where $U = D_c^{-1}$ and $\theta = \theta_c$, giving

$$\theta_c = D_c^{\gamma - 1}\theta_1 . \tag{2.20}$$

Substituting this in equation (2.13) now gives D_c in terms of γ and $\mathcal{M}_1$:

$$D_c^{\gamma + 1} - (1 + \gamma\mathcal{M}_1^2)D_c + \gamma\mathcal{M}_1^2 = 0. \tag{2.21}$$

Equation (2.21) has a unique root $D_c > 1$ for $\mathcal{M}_1 > 1$, $\gamma \geq 1$. For $\gamma = 1$, $D_c = \mathcal{M}_1^2$, as expected for an isothermal shock.

As noted above, the flow must pass through a sonic point, where the numerator and denominator of equation (2.16) both vanish. This condition, together with equation (2.19), gives U and θ at the sonic point (subscript asterisk):

$$U_* = b^{-1}, \quad \theta_* = (\gamma b^2)^{-1}, \tag{2.22}$$

where

$$b \equiv \frac{\alpha\delta}{\gamma} = \mathscr{M}_1^{2/(\gamma+1)}. \tag{2.23}$$

Making use of the sonic point has thus given us $\alpha\delta$ in terms of γ and $\mathscr{M}_1$.

To integrate equation (2.16) it is convenient to express the velocity in units of its value at the sonic point,

$$w \equiv U/U_* = bU, \tag{2.24}$$

and to rescale the nondimensional height:

$$x \equiv b^2\zeta. \tag{2.25}$$

The equation of motion (2.16) now becomes

$$\frac{dw}{dx} = \frac{w^\gamma - 1}{w^{\gamma+1} - 1}, \tag{2.26}$$

and is subject to boundary conditions

$$w(0) = a \equiv bD_c^{-1}, \quad w(x_0) = b, \tag{2.27}$$

where $x_0 = b^2\zeta_0$. Note that $\gamma \geq 1$ and $\mathscr{M}_1 > 1$ ensure that $a < 1$ and $b > 1$, so that a sonic point occurs at $w = 1$. Equation (2.26) may be integrated by quadratures, using w as independent variable (valid, since $dw/dx > 0$):

$$x(w) = \int_a^w \frac{y^{\gamma+1} - 1}{y^\gamma - 1}\, dy. \tag{2.28}$$

For rational γ the quadrature may be evaluated analytically; in general a numerical quadrature is performed. Equation (2.28) gives, in particular, the nondimensional separation between shocks, $\zeta_0 = b^{-2}x(b)$, in terms of γ and $\mathscr{M}_1$.

The last step remaining in the solution is to integrate equation (2.17) and to impose boundary conditions on the density (cf. eq. [2.12]):

$$\ln DU = \gamma \int_a^w \frac{y^{\gamma+1} - 1}{y^\gamma - 1}\frac{dy}{y}. \tag{2.29}$$

Evaluating D at $\zeta = \zeta_0$ ($w = b$) gives (cf. eqs. [2.14], [2.15])

$$\delta = \left[\int_a^b \frac{dx}{dw}\frac{dw}{b}\right]\left[\int_a^b \frac{dx}{dw}\frac{dw}{w}\right]^{-1}. \tag{2.30}$$

Clearly $0 < \delta < 1$, as expected ($v_s > 0 \Rightarrow \delta > 0$, $v_1 = v_s - u_1 < 0 \Rightarrow \delta < 1$). The full solution in the deceleration region is now given by equations (2.19)–(2.21) and (2.23)–(2.30). It is specified completely by giving γ plus one other parameter (e.g., $\mathscr{M}_1$, θ_1, θ_c), most conveniently taken to be the preshock Mach number $\mathscr{M}_1$.

Before graphically presenting the plane-parallel solutions, we derive the flux of radiation F_s emitted in the postshock radiative cooling layer as shocked gas cools to T_c. F_s follows from the mass and momentum shock jump conditions (2.11) and the energy jump condition

$$\frac{1}{2}u_c^2 + \frac{\gamma}{\gamma-1}\frac{p_c}{\rho_c} + \frac{F_s}{\rho_1 u_1} = \frac{1}{2}u_1^2 + \frac{\gamma}{\gamma-1}\frac{p_1}{\rho_1}, \tag{2.31}$$

where the subscript c refers to conditions at the base of the cooling region. Equation (2.31) is simply a statement of energy conservation, and gives F_s independently of how the cooling gas radiates. It is valid provided that preshock conditions are taken above the radiative precursor (if one exists), and that heat conduction and radiation pressure can be neglected (this is true here). While photons emitted in the postshock cooling layer may be absorbed higher in the atmosphere (cf. Fox, Wood, and Dopita 1984 for absorption of Balmer emission lines), this fact is accounted for by leaving the postshock adiabatic exponent γ a parameter to be determined, and otherwise has no effect on the jump conditions. Combining equations (2.11) and (2.31) now yields

$$\frac{F_s}{\rho_1 u_1^3} = \frac{1}{2}(1 - D_c^{-2}) - \frac{\gamma}{\gamma-1}(\theta_c - \theta_1). \tag{2.32}$$

The shock luminosity follows by multiplying F_s by the shock surface area. As we will see in § IV*d*, shock emission in Mira variables provides a substantial fraction of the visual luminosity at early phases.

Figure 2 is an Eulerian snapshot showing the distribution of fluid velocity, density, temperature, and pressure, for the plane-parallel case $\gamma = 1.10$, $\mathscr{M}_1 = 9$, corresponding approximately to R Cas and χ Cyg near maximum light (cf. § IV). Two shocks and three deceleration regions are shown. The zero point of z (or, equivalently, the phase) is arbitrary, since the formal solution extends over $-\infty < z < \infty$; of course, in a real star the shock forms first in some definite layer. To obtain the distributions at a later time, one simply shifts the curves to the right by v_s/h per unit time, while simultaneously lowering ln D and ln P by $\alpha v_s/h$ per unit time.

With $\gamma = 1.10$ and $\mathscr{M}_1 = 9$, numerical quadrature gives parameter values

$$D_c = 58.93, \quad \delta = 0.4198, \quad \zeta_0 = 0.6022, \quad \alpha = 21.24. \tag{2.33}$$

The radiative shocks compress the fluid by an amount D_c; we note from Figure 2 that this compression is superposed on a roughly exponential density distribution. (By comparison, for a hydrostatic, isothermal, plane-parallel atmosphere the density distribution is exactly exponential.) The temperature also jumps behind each shock, although not by a large factor here, since γ is close to unity. The velocity changes sign at the shocks, which convert infall ($v < 0$) into outflow ($v > 0$). The peak outflow velocity is less in magnitude than the peak infall velocity by a factor of $(\delta - D_c^{-1})/(1 - \delta) = 0.6944$. In the limit $\mathscr{M}_1 \to \infty$, this ratio approaches unity.

Figure 2 may be compared with the isothermal numerical simulations of Wood (1979, Fig. 7; see also Figs. 11–13 below). The velocity and density profiles are qualitatively similar, although in Wood's models the shock velocity and separation between shocks decrease with height. The difference occurs primarily because of our plane-parallel assumption. Since (for fixed γ and $\mathscr{M}_1$) $v_s \propto gP$, $h \propto v_s P$, and $g \propto r^{-2}$, we may anticipate that the shock velocity and separation will decrease with height when spherical effects are included (§ III).

The plane-parallel solution is particularly simple in the limit of a strong shock, $\mathscr{M}_1 \gg 1$. We then have (cf. eq. [2.33])

$$D_c \approx \theta_c^{-1} \approx (\gamma\mathscr{M}_1^2)^{1/\gamma}, \quad \delta \approx \zeta_0 \approx \tfrac{1}{2}, \quad \alpha \approx 2\gamma\mathscr{M}_1^{2/(\gamma+1)}. \tag{2.34}$$

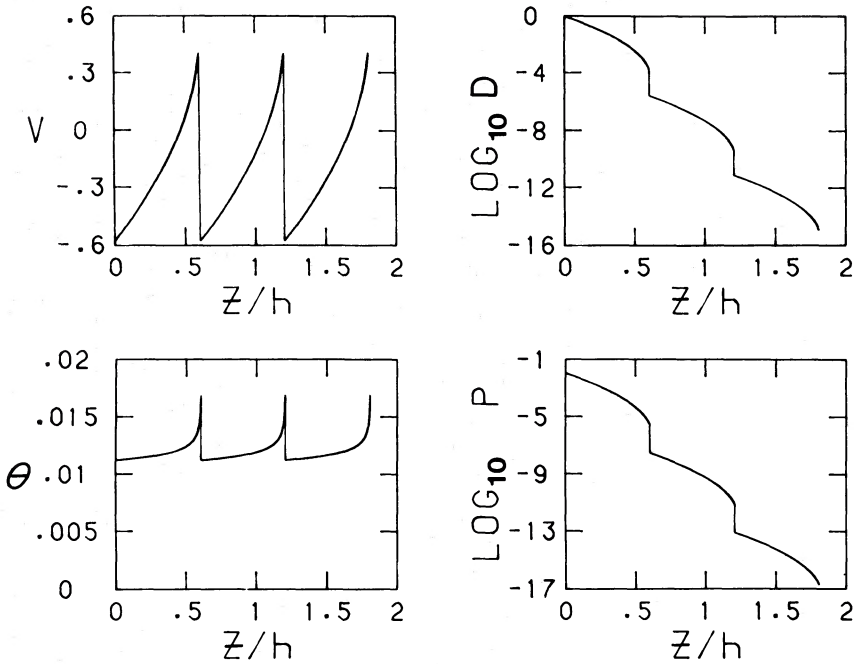

FIG. 2.—Eulerian view of the plane-parallel periodic shock model showing the nondimensional fluid velocity V, density D, temperature θ, and pressure P (see eq. [2.6] for units) vs. height z/h. The model shown here assumes shock Mach number $\mathscr{M}_1 = 9$ and postshock adiabatic exponent $\gamma = 1.10$, roughly appropriate for χ Cyg and R Cas near maximum light.

The separation between shocks is just $\zeta_0 h = \frac{1}{2}u_1^2/g$, while the preshock density scale height is $h/\alpha(1/2\gamma)(\gamma b)^{1/\gamma}C_c^2/g$. By contrast, the density scale height for a hydrostatic, isothermal, plane-parallel atmosphere is C^2/g. The atmospheric structure is changed considerably when shocks, and not hydrostatic pressure gradients, provide the support. Strong shocks ($b \gg 1$) increase the scale height and thus increase the density over that in a static atmosphere. Note also that for $\mathscr{M}_1 \gg 1$ the upward shock velocity equals in magnitude the preshock velocity, when both are measured in the stellar rest frame. The limit $\mathscr{M}_1 \gg 1$ is just the "ballistic" limit of Hill and Willson (1979), in which pressure forces are unimportant. This is because pressure forces are important only above the sonic point, which occurs close behind the shock: $\zeta_* \sim (\gamma\mathscr{M}_1^2)^{-2/(\gamma+1)} \ll \zeta_0$. For $\mathscr{M}_1 \gg 1$ shocked fluid elements fly upward and back on essentially ballistic (freely falling) trajectories.

We have obtained the Eulerian solution for the fluid motion, but it is also useful to have the Lagrangian description giving the motion of a fixed fluid element. This is necessary in particular to derive the period P in terms of quantities defined above. To derive the trajectory of a fluid element, we integrate its equation of motion,

$$\frac{dz}{dt} = v = u_1(\delta - U) . \tag{2.35}$$

The solution may be written parametrically:

$$z = z_0 + h(\delta\tau - \zeta) , \quad t = t_0 + \frac{h}{u_1}\tau , \tag{2.36}$$

where

$$\zeta(w) = b^{-2}x(w) , \quad \tau(w) = b^{-1}\int_a^w \frac{y^{\gamma+1} - 1}{y^\gamma - 1}\frac{dy}{y} . \tag{2.37}$$

The fluid element is shocked at $z = z_0$, $t = t_0$, $w = a$, and returns to be shocked one period later, at $z = z_0$, $t = t_0 + P$, $w = b$. Using equations (2.30), (2.36), and (2.37), we obtain the period:

$$P = \frac{\zeta_0}{\delta}\frac{h}{u_1} . \tag{2.38}$$

For a strong shock, $\delta \approx \zeta_0 \approx \frac{1}{2}$ (eq. [2.34]), giving the standard result $v_s = gP/2$ for ballistic trajectories.

Figure 3 shows a series of shock lines and particle trajectories in a spacetime diagram plotting height versus phase,

$$\phi \equiv \frac{t - t_0}{P} = \frac{\delta\tau}{\zeta_0} , \tag{2.39}$$

for the case $\gamma = 1.10$, $\mathscr{M}_1 = 9$. For these values $P = 1.434h/u_1$. As in Figure 2, the zero points of z and ϕ are arbitrary; the trajectories for different particles may be obtained simply by varying z_0 or t_0. The shock lines are straight because in the plane-parallel solution the shock velocity is independent of height; consequently the particle trajectories are identical except for the shift along the shock lines. Note that because the shock compression is so large (eq. [2.33]), the postshock particle velocity very nearly equals the shock velocity: $\delta - D_c^{-1} \approx \delta$. Because $\mathscr{M}_1$ is large, the particle trajectories deviate little from ballistic trajectories $z = z_0 + \frac{1}{2}gP^2\phi(1 - \phi)$.

Now that we have the trajectories of individual fluid particles, it is also possible to compute the Lagrangian fluid distributions, i.e., the velocity, density, temperature, and pressure following a fixed fluid element. Parameterizing the solution by w, we obtain

$$V(w) = \delta - U , \quad D(w) = U^{-1} , \quad \theta(w) = \theta_1 D^{\gamma-1} ,$$
$$P(w) = \theta_1 D^\gamma , \tag{2.40}$$

where D and P are normalized in terms of the preshock density and pressure seen by the given particle. The results are plotted

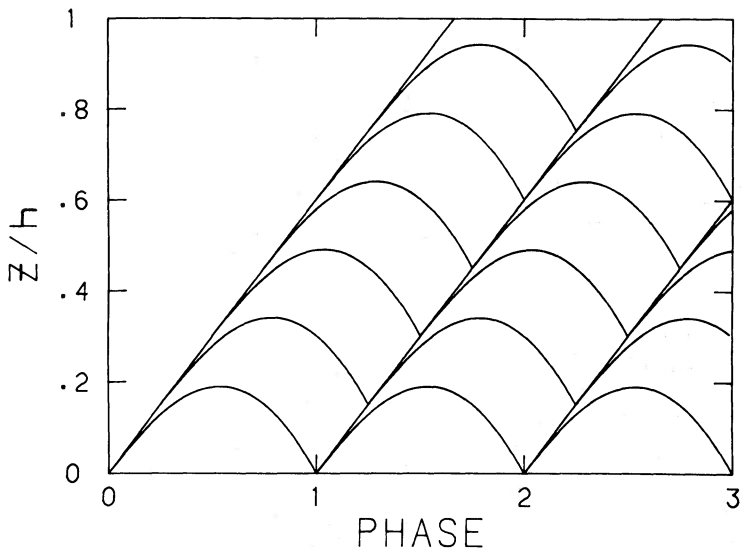

FIG. 3.—Spacetime diagram for the model atmosphere of Fig. 2. The straight lines show the upward propagation of shocks with increasing phase. The oscillating curves give the trajectories of selected fluid elements. Each element is propelled upward by the shock and postshock pressure forces, but eventually falls back because of gravity.

against time (phase) in Figure 4, again with $\gamma = 1.10$, $\mathcal{M}_1 = 9$. The fluid element passes through the sonic point at $\phi = 0.235$. At later phases pressure forces become negligible, and the fluid element decelerates uniformly with $dv/dt = -g$. The mass flux in the shock frame following the element is constant, $DU = 1$, because in this frame the nondimensionalized flow is steady. The postshock flow is adiabatic, hence $P \propto D^{\gamma}$, $\theta \propto D^{\gamma-1}$. Because the preshock density decreases with height, however, different fluid elements are on different adiabats.

As noted above, the plane-parallel assumption is violated for Mira variables. The assumption is valid if and only if the separation between shocks is much less than the stellar radius, or $h/R \ll 1$. A simple estimate shows this requirement to be violated for long-period variables:

$$\frac{h}{R} = \left(\frac{\delta}{\zeta_0}\frac{Pu_1^3}{GM}\right)^{1/2} = 0.49\left(\frac{\delta}{\zeta_0}\right)^{1/2}\left(\frac{u_1}{10\ \mathrm{km\ s^{-1}}}\right)^{3/2}\left(\frac{P/\mathrm{yr}}{M/M_\odot}\right)^{1/2}. \quad (2.41)$$

Since Mira variables have $P \sim 1$ yr and $M \sim M_\odot$, and observations indicate that $u_1 \sim 30$ km s^{-1} in the deeper parts of the atmosphere (Hinkle, Hall, and Ridgway 1982; Hinkle, Schar-

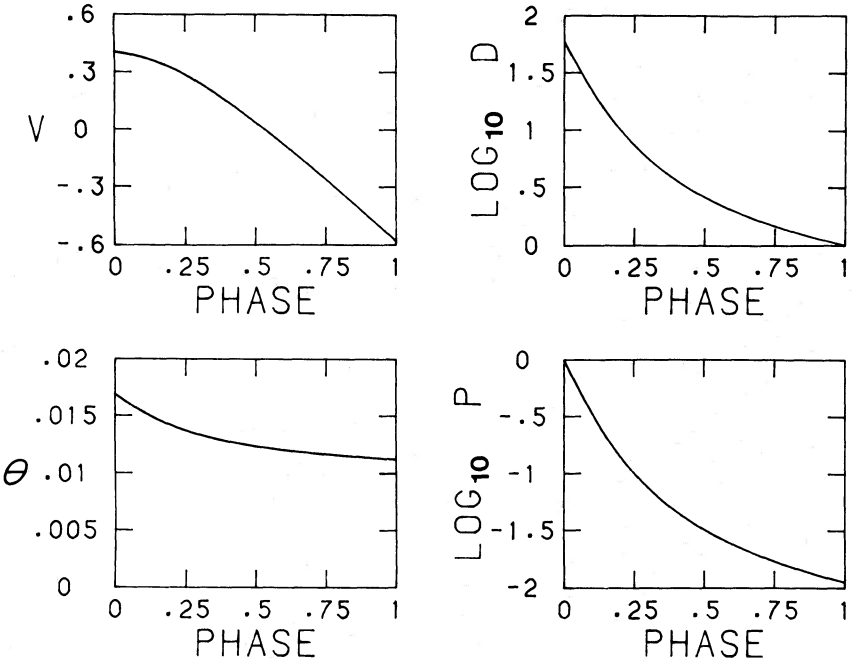

FIG. 4.—Lagrangian view of the model atmosphere of Fig. 2, showing the variation of the fluid variables along a fixed particle trajectory

lach, and Hall 1984), the plane-parallel assumption is clearly violated. The implications are that (1) the shock velocity is a significant fraction of the escape velocity v_e, since

$$\left(\frac{v_s}{v_e}\right)^2 = \frac{\delta^2}{2}\frac{h}{R}, \tag{2.42}$$

and (2) the vertical amplitude of a particle trajectory is not small compared with its radius. Under these conditions it is inappropriate to assume g = constant.

III. SPHERICAL PERIODIC SHOCKS

In this section we generalize the plane-parallel periodic shock solution derived above to include spherical effects. In contrast to § II, here we allow T_c, μ, and γ to vary with Lagrangian radius, but we do not assume any particular functional dependence. We will assume throughout that the atmosphere contributes a negligible amount of mass to the star, so that we may set M = constant. Later this assumption will be verified from model fits to stars. As in § II, we choose to work in the shock frame, but now we can no longer assume that the shock velocity is constant.

We make the following definitions, all generalizations of the plane-parallel case. The shock radius measured from the center of the star is $r_s(t)$. The shock velocity is $dr_s/dt = v_s(t)$, and the preshock fluid speed in the shock frame is $u_1(t) = v_s(t)/\delta(t)$. The escape velocity from height r_s is

$$v_e(t) \equiv \left(\frac{2GM}{r_s}\right)^{1/2} \equiv \frac{v_s(t)}{\beta(t)}. \tag{3.1}$$

If $\beta > 1$, a particle at height r_s moving with speed v_s will be unbound. [This definition of β differs from that of Hill and Willson 1979, who used the postshock fluid velocity v_c rather than v_s. The two definitions differ by a factor of $v_c/v_s = 1 - 1/(\delta D_c)$; for the values in eq. (2.33) this factor is 0.96.] The effective gravitational deceleration measured in the shock frame is

$$g(t) \equiv \frac{GM}{r_s^2} + \frac{dv_s}{dt} = \frac{1}{2}\frac{v_e^2}{r_s}\chi, \tag{3.2}$$

where

$$\chi(t) \equiv 1 + 2\beta^2\frac{d\ln v_s}{d\ln r_s}. \tag{3.3}$$

The second term of equation (3.2) (dv_s/dt) arises because the shock frame is accelerating. Again we define the scale height $h(t) \equiv u_1^2/g$; it follows that

$$\frac{h}{r_s} = \frac{2\beta^2}{\chi\delta^2}. \tag{3.4}$$

The preshock density, pressure, and Mach number are, respectively, $\rho_1(t)$, $p_1(t)$, and $\mathcal{M}_1(t)$.

The independent variables are transformed from (r, t) to (ζ, τ), where

$$r = r_s(t) - h(t)\zeta, \quad dt = \frac{h(t)}{u_1(t)}d\tau. \tag{3.5}$$

The dependent fluid variables v, ρ, p, and T are nondimensionalized as in equation (2.6), but with u_1 and ρ_1 functions of time (or shock height r_s). Nondimensionalizing the fluid equations (2.1)–(2.3) now yields

$$\frac{\partial D}{\partial\tau} + \left(U - \zeta\frac{\dot h}{u_1}\right)\frac{\partial D}{\partial\zeta} + D\left(\frac{\partial U}{\partial\zeta} + 2\frac{h}{r_s}\frac{\delta - U}{1 - \zeta\dot h/u_1}\right) = \alpha\delta D, \tag{3.6}$$

$$\frac{\partial U}{\partial\tau} + \frac{h}{r_s}\frac{d\ln u_1}{d\ln r_s}\delta U + \left(U - \zeta\frac{\dot h}{u_1}\right)\frac{\partial U}{\partial\zeta} + \frac{1}{D}\frac{\partial P}{\partial\zeta} = 1 - \frac{\zeta}{\chi}\frac{h}{r_s}\left(2 - \zeta\frac{h}{r_s}\right), \tag{3.7}$$

$$\frac{\partial P}{\partial\tau} + 2\frac{h}{r_s}\frac{d\ln u_1}{d\ln r_s}\delta P + \left(U - \zeta\frac{\dot h}{u_1}\right)\frac{\partial P}{\partial\zeta} + \gamma P\left(\frac{\partial U}{\partial\zeta} + 2\frac{h}{r_s}\frac{\delta - U}{1 - \zeta\dot h/u_1}\right) = \alpha\delta P, \tag{3.8}$$

where

$$\alpha(t) \equiv -\frac{h}{r_s}\frac{d\ln\rho_1}{d\ln r_s}. \tag{3.9}$$

The nondimensional fluid equations (3.6)–(3.8) must satisfy boundary conditions imposed by periodicity, and the radiative shock jump conditions equations (2.11). Assuming that the cooling region is much thinner than r_s, or equivalently that $t_{\rm cool} \ll P$, equations (2.12) and (2.13) must hold in the spherical case too. Equations (2.20) and (2.21) also hold, provided that $\mathcal{M}_1$, D, and θ are referred to the shock about to be crossed by a fluid element, not the shock crossed one period ago, which is higher up in the atmosphere. To justify the application of equations (2.20) and (2.21) here, we note that periodicity and zero mass loss require preshock gas to be on the same adiabat as gas that has just cooled, leading to equation (2.20). Since the fluid flow is adiabatic after cooling, if a fluid element had a different specific entropy after cooling than it had before being shocked, its entropy would be different after one period, and it could not return to its initial density, radius, and velocity, as demanded by strict periodicity. This same argument applies in the planar case, where it leads to equations (2.19) and (2.20). (Eq. [2.19] is just the entropy integral of the planar fluid equations.) Given equations (2.12), (2.13), (2.20), and (2.21), we can now specify boundary conditions at $(\zeta = 0^+, \tau)$ (i.e., at the bottom of the cooling region) in terms of γ and $\mathcal{M}_1(t)$. Note that γ may depend on the height at which a fluid element is shocked, i.e., its Lagrangian radius. (We do restrict γ to be constant for a given fluid element, however.)

Boundary conditions at the bottom of the deceleration region are not as simple here as equations (2.14), however, because, by the time a fluid element encounters the next shock, the velocity, preshock density, and so on, of the upper shock (in terms of which the fluid variables are nondimensionalized) may be quite different from those of the lower shock. Also, the boundary conditions are time dependent. Unfortunately we see no way to remove this time dependence and analytically integrate equations (3.6)–(3.8), as was done in the plane-parallel case.

Although an analytic solution of equations (3.6)–(3.8) seems impossible, an approximate solution may be obtained that should be sufficiently accurate for our purposes. The method of approximation, in brief, is to use the analytic plane-parallel solution for the postshock flow until pressure forces are negli-

gible, and thereafter to treat the motion as ballistic. A Lagrangian approach is adopted. For a particle crossing the shock at (r_0, t_0), the plane-parallel solution will give the correct trajectory for a short distance behind the shock, provided that the shock velocity, Mach number, cooling sound speed, and so on, are not varying too rapidly as the shock propagates upward, so that they may be approximated by their values at $r_s = r_0$. Specifically, we require the three conditions

$$\left|\frac{d \ln (u_1, D_c, \theta_c)}{d \ln r_s}\right| \ll \left|\frac{d \ln \rho_1}{d \ln r_s}\right| \tag{3.10}$$

to be satisfied. The logarithmic derivatives on the left-hand side are all of order unity, since r_s provides the only scale on which u_1, D_c, and θ_c can vary. If equations (3.10) are satisfied, then all the time-dependent and spherical terms in equations (3.6)–(3.8) may be neglected for postshock distances ζh satisfying

$$\zeta h \ll \chi r_s . \tag{3.11}$$

Equation (3.11) is equivalent to the requirement that a particle not rise a significant fraction of its original height r_0 during the interval of planar approximation.

Applying the plane-parallel solution reduces equations (3.10) and (3.11) to the two conditions

$$1, w \ll \frac{\delta \chi b}{\beta} , \tag{3.12}$$

where $w = U/b$ parameterizes the planar solution (cf. § II), and δ, χ, $b \equiv \mathscr{M}_1^{2/(\gamma+1)}$, and β are evaluated at $r_s(t_0) = r_0$. To be certain of satisfying equations (3.12) we will apply the planar solution only for

$$a \le w \le w_{\max} \equiv \left(\frac{\delta \chi b}{2\beta^2}\right)^{1/2} . \tag{3.13}$$

The method of approximation used here is good for $w_{\max} \gg 1$, so that (1) the planar treatment is valid for $w < w_{\max}$ and (2) the ballistic trajectory treatment is valid at later phases, since the sonic plant is at $w = 1$ and pressure forces can be neglected along a trajectory for $w \gg 1$. If $w_{\max} > b$, then the planar solution is used along the entire trajectory. We do not know *a priori* whether $w_{\max} \gg 1$ will be satisfied in any given variable star; we will discover below (§ IV) that this condition is weakly satisfied for Mira variables.

To apply the planar solution, we need $\mathscr{M}_1$, β, δ, χ, D_c, etc., which depend on the unknown shock velocity and height. To obtain these quantities, we first note that the only independent model parameters describing a variable star atmosphere are γ, GM, P, C_c, and v_s. (The shock radius and velocity are not independent, since the solution will relate them.) From these quantities we can form exactly three independent dimensionless parameters:

$$\gamma , \quad \kappa \equiv \frac{PC_c^3}{GM} , \quad \lambda \equiv \frac{Pv_s^3}{GM} . \tag{3.14}$$

All three of these quantities may vary with shock height r_s. The problem is now formulated as follows: given γ, κ and λ, find $\mathscr{M}_1$, β, and $d \ln v_s/d \ln r_s$. All other quantities then follow. For example, the shock radius is

$$r_s = 2\beta^2 \frac{GM}{v_s^2} = 2\beta^2 \lambda^{-2/3} (GMP^2)^{1/3} . \tag{3.15}$$

Equation (3.15) enables us to determine the shock trajectory $r_s(t)$ by integrating the equation of motion

$$\frac{dr_s}{dt} = v_s = \lambda^{1/3} \left(\frac{GM}{P}\right)^{1/3} . \tag{3.16}$$

We impose the constraint that the trajectory must give $d \ln v_s/d \ln r_s$ self-consistently; this constraint will effectively determine χ (eq. [3.3]). Next, the preshock velocity in the shock frame is $u_1 = v_s/\delta$, where δ follows from $\theta_c = (C_c/u_1)^2$ and equations (3.14):

$$\delta = \left(\frac{\lambda}{\kappa}\right)^{1/3} \theta_c^{1/2} ; \tag{3.17}$$

equations (2.20) and (2.21) determine D_c and θ_c from γ and $\mathscr{M}_1$. Note that δ is not given by equation (2.30) because the planar solution is not necessarily valid everywhere. Finally, the preshock density distribution $\rho_1(r_s)$ follows up to a constant multiplicative factor from equation (3.9); α is given by equation (2.23), since we assume that the planar solution is valid at least through the sonic point $w = 1$. In short, once we know γ, κ, λ, $\mathscr{M}_1$, and β, we have the complete solution, provided that $w_{\max} \gg 1$.

To obtain $\mathscr{M}_1$ and β from γ, κ, and λ, and to obtain the fluid motion for $w > w_{\max}$, we need the ballistic particle trajectories. The trajectories follow from integrating Newton's law

$$\frac{d^2 r}{dt^2} = -\frac{GM}{r^2} , \tag{3.18}$$

with initial conditions provided by the Lagrangian formulation of the plane-parallel solution at $w = w_{\max}$. The solution to equation (3.18) may be written in the parametric form (θ should not be confused here with the nondimensional temperature of § II)

$$r = (GMP^2)^{1/3} x(\theta) , \quad t = t_0 + P\phi(\theta) , \tag{3.19}$$

where

$$x = \frac{1}{\epsilon} \sin^2 \theta , \quad \frac{dx}{d\phi} = \left(\frac{GM}{P}\right)^{-1/3} \frac{dr}{dt} = (2\epsilon)^{1/2} \cot \theta ,$$

$$(\phi - \phi_2)(2\epsilon^3)^{1/2} = \theta - \theta_2 - \frac{1}{2}(\sin 2\theta - \sin 2\theta_2) . \tag{3.20}$$

Since pressure forces are negligible, the nondimensional particle binding energy is

$$\epsilon \equiv \frac{1}{x} - \frac{1}{2}\left(\frac{dx}{d\phi}\right)^2 \tag{3.21}$$

and is constant for a particle during the ballistic phase. Initial conditions $x(\theta_2) \equiv x_2$, $\phi(\theta_2) \equiv \phi_2$, and $dx/d\phi(\theta_2) = 1 - U_2/\delta = 1 - w_{\max}/b\delta$ are provided by the planar trajectory (eqs. [2.36] and [2.37], with z replaced by r), evaluated at $w = w_{\max}$. All shock parameters (a, b, h, δ, u_1, C_c, etc.) are evaluated when the particle crosses the shock at $r_s(t_0)$. As shown above, these parameters follow from GM, P, γ, κ, λ, $\mathscr{M}_1$, and β.

Finally, we can obtain $\mathscr{M}_1$ and β from γ, κ, and λ. There are two constraints that must be imposed on the ballistic trajectories: after one period, a particle must return (1) to its original position, (2) with its original preshock velocity. These conditions follow from the assumptions of periodicity with no mass

loss. They may be written

$$(2\epsilon)^{1/2} \cot \theta_1 = \lambda^{1/3}(\delta - 1)/\delta \quad (3.22)$$

and

$$(1 - \phi_2)(2\epsilon^3)^{1/2} = \theta_1 - \theta_2 - \tfrac{1}{2}(\sin 2\theta_1 - \sin 2\theta_2)\,, \quad (3.23)$$

where

$$\theta_1 = \pi - \arcsin\,[(\epsilon x_0)^{1/2}]\,, \quad (3.24)$$

with x_0 following from equation (3.19) ($r = r_0$). Evaluating the first of equations (3.20) at $x = x_2$ gives θ_2. Equations (3.22) and (3.23) implicitly relate γ, κ, λ, $\mathcal{M}_1$, and β, since ϵ, θ_1, δ, etc., all follow once these quantities are known. It can be shown numerically that, given γ, κ, and λ, equations (3.22) and (3.23) uniquely determine $\mathcal{M}_1$ and β, so the shock model is unique.

Equations (3.13)–(3.24), plus the relevant equations of § II, determine the spherical periodic solution, i.e., they give the atmospheric structure for a variable star with shocks once γ, M, P, and C_c are specified. (It is necessary to give the dependence of γ and C_c on Lagrangian radius to obtain the solution over a similar range in radius.) They do not fix the minimum shock radius (this follows from stellar pulsation theory; cf. Keeley 1970 and Wood 1974) or the unit of density (since the density is determined only up to a constant multiplicative factor), but these may be inferred from observations (cf. § IV). The constraint equations (3.22) and (3.23) are implicit, so that an explicit solution is not possible, but an accurate numerical solution using Newton-Raphson iteration is easy to obtain. The solution procedure amounts to varying $\mathcal{M}_1$ and β until equations (3.22) and (3.23) are satisfied, for given γ, κ, and λ. This gives the solution at a height r_s given by equation (3.15). We then decrease λ slightly and change γ and C_c as necessary and repeat the procedure to obtain the solution at a higher altitude, checking to ensure that $d \ln v_s/d \ln r_s$, approximated by finite differences, satisfies equation (3.3) for χ; this condition requires an additional Newton-Raphson iteration. This procedure is repeated varying r_s to obtain the solution over any desired range in radius. As noted above, a given star will have a minimum r_s below which shocks do not appear; it will also have a maximum r_s above which mass loss ruins the assumption of periodic orbits.

Obtaining a periodic shock solution requires specifying $\gamma(r_s)$ and $\kappa(r_s)$, which depend on thermodynamic properties of the stellar atmosphere. In principle they can be determined theoretically, but this requires calculating the details of shock structure, gas properties, and radiative transfer. The purpose of our model is to give a reasonable description of a Mira atmosphere without such a complicated treatment. Fortunately γ and C_c can be determined empirically (§ IV), although present observations fix them at only one point in radius. Lacking complete knowledge of the thermodynamics, however, we still find it useful to make reasonable guesses about their dependence on height.

In Figures 5–8 we plot fundamental quantities for the spherical periodic shock solution, where we have made the simplest possible assumption about γ and C_c, i.e., that they are independent of height. We fix them at values given by model fits to a deep atmospheric layer of χ Cyg (§ IV), $\gamma = 1.10$ and $\kappa = 0.0175$. The small glitches present in the curves occur where $w_{\max} = b$, and are due to our approximate method of solution. The entire solution may be derived as described above from Figures 5 and 6. Figure 5 graphs the shock Mach number versus $\lambda/\kappa = (v_s/C_c)^3$ (rather than λ) because an increase in κ can nearly be compensated for by a proportionate increase in λ. Figure 6 graphs the ratio β of shock velocity to escape velocity as a function of λ. Varying κ affects Figures 5 and 6, but only for small Mach number; this is because, by definition, κ measures the relative importance of gas pressure in the deceleration region (cf. eq. [3.14]), and pressure forces are unimportant for $\mathcal{M}_1 \gg 1$. Varying γ changes $\mathcal{M}_1$ slightly, but both β and the shock compression D_c (which depends on $\mathcal{M}_1$ and γ) are practically independent of γ. Thus Figures 5 (with D_c instead of $\mathcal{M}_1$) and 6 may be applied to widely different cases of γ and κ, with errors of a few percent or less for

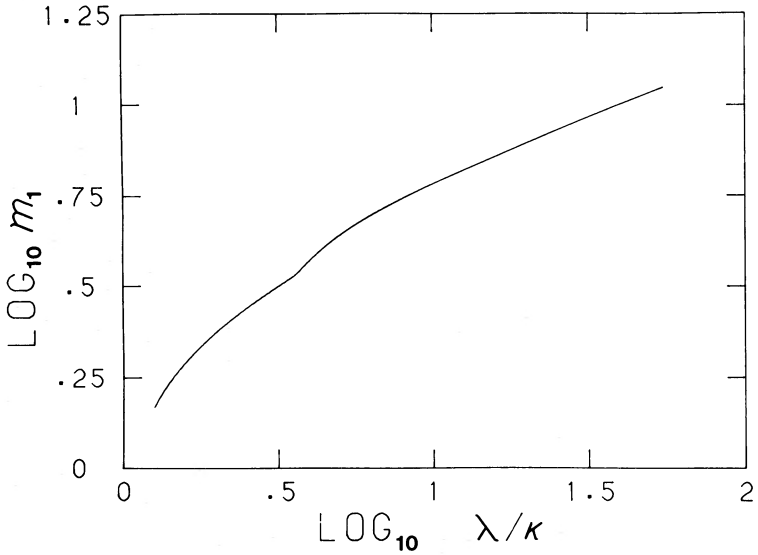

FIG. 5.—Dependence of shock Mach number $\mathcal{M}_1$ on $\lambda/\kappa = (v_s/C_c)^3$ for the spherical periodic shock model with thermodynamic parameters $\gamma = 1.10$, $\kappa = 0.0175$, appropriate for the deep layers of χ Cyg. The assumption of constant γ and κ (independent of height) used here is unrealistic, but for large $\mathcal{M}_1$ this figure can be applied for varying γ and κ, as described in the text.

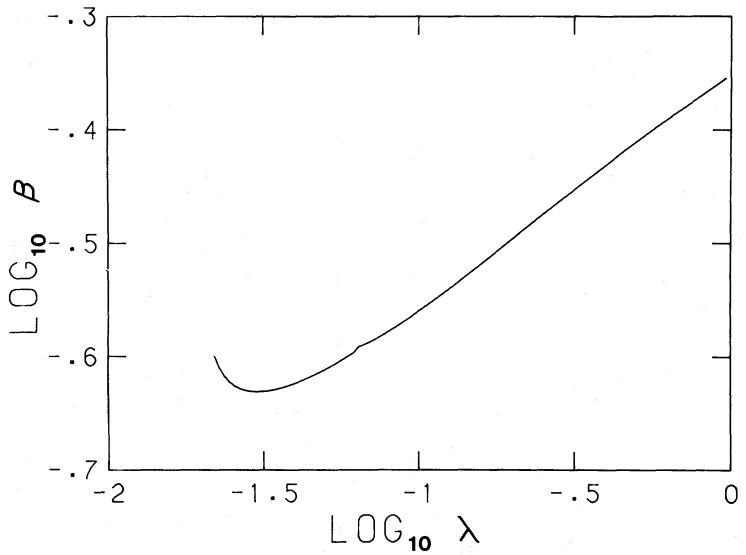

FIG. 6.—The ratio β of shock velocity to escape velocity, as a function of $\lambda \equiv Pv_s^3/GM$, for the same solution as in Fig. 5. Fluid elements are bound for $\beta < 1$. This figure is insensitive to the values of γ and κ, except at small v_s ($\lambda < 0.1$).

$\mathcal{M}_1 > 3$. This implies that although the thermodynamic variables (p, T) are sensitive to γ and κ, the fluid trajectories are not, so long as the shock is strong.

Although κ and λ are convenient quantities to parameterize the spherical solutions, it is physically more useful to plot $\mathcal{M}_1$ and β against radius instead, as in Figures 7 and 8. The unit of radius is (eq.[3.15])

$$[r] = (GMP^2)^{1/3} = 5.094 \times 10^{13}\left(\frac{M}{M_\odot}\right)^{1/3}\left(\frac{P}{\text{yr}}\right)^{2/3} \text{ cm} . \quad (3.25)$$

Figure 7 shows that, as a shock propagates up through a Mira variable atmosphere, it weakens, if constant cooling sound speed is assumed. (The shock will weaken in general if the preshock sound speed, or equivalently C_c, does not decrease too rapidly with radius.) Because C_c is here a constant but v_e decreases with r (eq. [3.1]), a sonic point exists (where $\mathcal{M}_1 = 1$), beyond which the flow cannot support a periodic shock and must turn into a wind. The rapid radiative cooling assumption is likely to break down interior to this, however, moving the sonic radius further in.

Figure 8 shows the variation of β with radius. At small r, β approaches 1 and particle orbits become very extended. With increasing radius, β first decreases, since the shock velocity decreases more rapidly than $r^{-1/2}$. But if and when the shock becomes weak, pressure forces keep v_s from falling as rapidly as v_e, and β increases again. The minimum in β becomes deeper and shifts to increasing r as κ is decreased, because pressure forces are then less important. Note that β is not constant, as was suggested by Hill and Willson (1979) on the basis of numerical simulations. [Adopting their definition $\beta = v_c/v_e$ makes the variation of β with radius shown in Fig. 8 even greater, because $D_c = v_s/(v_s - v_c)$ decreases with increasing radius.] They pointed out that constant β would lead to mass loss because beyond some radius gravitational forces could not

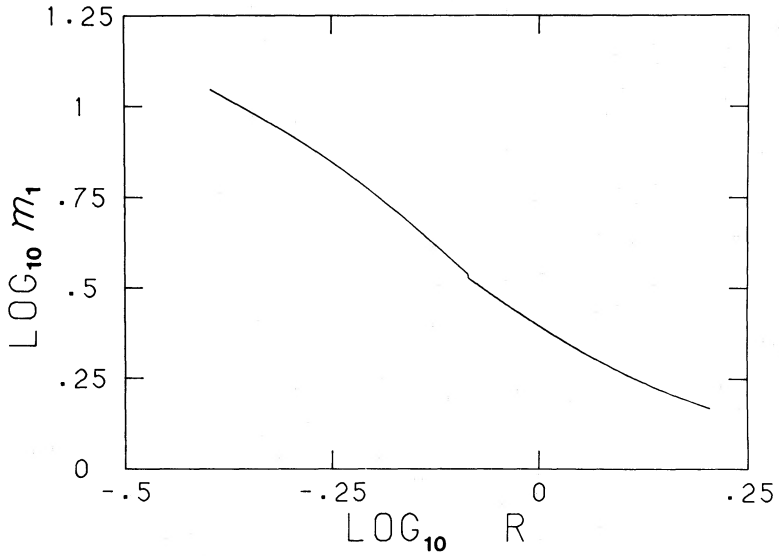

FIG. 7.—Same as Fig. 5, except that $\mathcal{M}_1$ is plotted vs. radius, with units given by eq. (3.25). The shock would not weaken so rapidly with radius had we assumed more realistically that the isothermal cooling sound speed C_c decreases with radius.

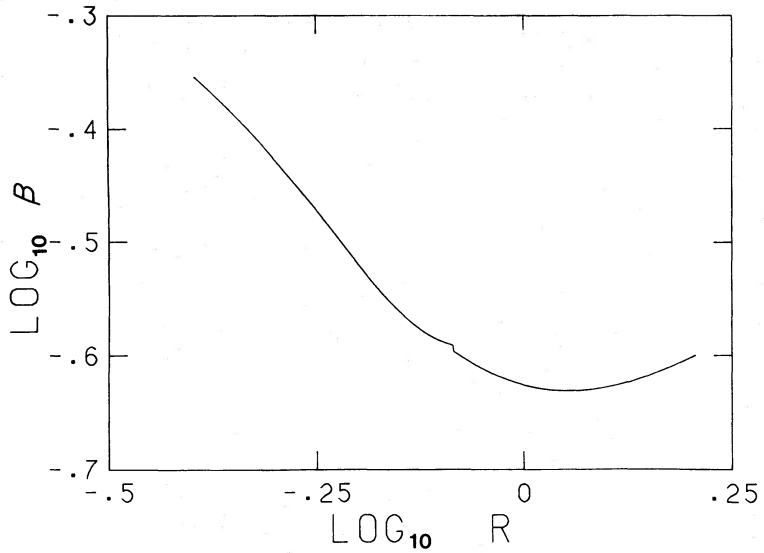

FIG. 8.—Same as Fig. 6, except that β is plotted vs. radius, with units given by eq. (3.25). At small radius $\beta \rightarrow 1$.

then return a particle to its initial radius in one period. However, this cannot be considered as a physical mechanism for mass loss (Willson and Hill 1979), because there is no *a priori* reason that β should be constant.

So far we have derived the Lagrangian solution for the motion (i.e., fluid trajectories) of periodically shocked gas in the spherical case, but not the thermodynamic quantities. Since the postshock motion of a fixed fluid element is assumed to be adiabatic, these all follow from the density ρ. For $w < w_{\max}$, when the planar solution is used, the density along a particle orbit is just given by equation (2.40). We now derive the density in the ballistic phase of motion, when the trajectories are given by equations (3.19)–(3.21).

Consider two mass shells, one crossing the shock at (r_0, t_0), and the other, at $(r_0 + dr_0, t_0 + dt_0)$, where $dr_0 = v_s dt_0$. Let dr be the vertical separation (at fixed time) between the shells. Since the shells cannot cross, conservation of matter implies

$$\rho r^2 dr = \text{const.} = \rho_1 r_0^2 \frac{dr_0}{\delta}, \tag{3.26}$$

where ρ is the density at (r, t), and $\rho_1 = \rho(r_0, t_0)$ is the preshock density. The factor $1/\delta$ appears because the upper shell is still falling in (with speed v_s/δ in the shock frame) when the lower shell is shocked. Thus the density along a particle trajectory follows once the orbits $r(t)$ and hence separation between adjacent particles are known.

Equations (3.19)–(3.21) give the particle trajectories in the ballistic phase, which may be written implicitly $r = r(r_0, \phi)$, where ϕ measures time along the orbit of a particle with Lagrangian coordinate r_0, the height at which it is shocked. Since $dr_0 = v_s dt_0$ and the particle velocity is $v = (1/P)(\partial r/\partial\phi)_{r_0}$, equation (3.26) becomes

$$\left(\frac{\rho}{\rho_1}\right)^{-1} = \delta\left(\frac{r}{r_0}\right)^2\left[\left(\frac{\partial r}{\partial r_0}\right)_\phi - \frac{v}{v_s}\right]. \tag{3.27}$$

To compute the partial derivative in equation (3.27), we note that equations (3.19)–(3.21) are written in the form $r = r(r_0, \theta)$, $\phi = \phi(r_0, \theta)$, since ϵ and θ_1 are functions of r_0. (For convenience we use the difference between expressions eqs. [3.20] and [3.23], not eq. [3.20], to give ϕ in terms of θ, ϵ, and θ_1.) We thus have

$$\left(\frac{\partial r}{\partial r_0}\right)_\phi = \left(\frac{\partial r}{\partial r_0}\right)_\theta + \left(\frac{\partial r}{\partial \theta}\right)_{r_0}\left(\frac{\partial \theta}{\partial r_0}\right)_\phi, \tag{3.28}$$

where

$$\left(\frac{\partial \theta}{\partial r_0}\right)_\phi = -\left(\frac{\partial \phi}{\partial r_0}\right)_\theta\left(\frac{\partial \phi}{\partial \theta}\right)_{r_0}^{-1}. \tag{3.29}$$

The desired partial derivatives are

$$\left(\frac{\partial r}{\partial r_0}\right)_\theta = -\frac{r}{\epsilon}\frac{d\epsilon}{dr_0}, \quad \left(\frac{\partial r}{\partial \theta}\right)_{r_0} = \frac{\sin 2\theta}{\epsilon},$$
$$\left(\frac{\partial \theta}{\partial r_0}\right)_\phi = \frac{r_0}{r}\frac{d\theta_1}{dr_0} + \frac{3}{2}(2\epsilon)^{1/2}\frac{(\phi - 1)}{r}\frac{d\epsilon}{dr_0}. \tag{3.30}$$

The total derivatives $d\epsilon/dr_0$ and $d\theta/dr_0$ are obtained by numerically differentiating the solutions obtained earlier, since all quantities are tabulated as a function of shock height. The preshock density is given up to a normalizing factor by integrating equation (3.9); the normalization will be computed in § IV*c* from observed absorption-line column densities. The pressure and temperature measured along a particle orbit follow simply from adiabaticity, e.g.,

$$T = \frac{\mu u_1^2}{k}(\gamma M_1^2)^{-1}\left(\frac{\rho}{\rho_1}\right)^{\gamma - 1}. \tag{3.31}$$

Once the Lagrangian solution is known, giving the variation of the fluid variables along particle trajectories, the Eulerian solution may be derived, giving the variation with height at fixed time. The procedure is simply along each trajectory to invert the relation $t = t_0 + h\tau(w)/u_1$ to give $w = w(\tau)$ (eq. [2.36], for the plane-parallel portion of a trajectory), or $t = t_0 + P\phi(\theta)$ to give $\theta = \theta(\phi)$ (eq. [3.19], for the ballistic portion of a trajectory). These inversions are performed numerically using Newton-Raphson iteration. We will present graphs of the Lagrangian and Eulerian fluid distributions in § IV, where the results of this section are applied to fit infrared spectral line observations.

IV. COMPARISON OF SHOCK MODELS WITH OBSERVATIONS

Until recently, observations of Mira variables have not warranted a complex theoretical model of their atmospheric structure like that presented in §§ II and III, although useful numerical hydrodynamical simulations have been made (Wood 1979; Willson and Hill 1979). The situation has changed completely with infrared spectroscopy by Hinkle and his coworkers (Hinkle 1978; Hinkle and Barnes 1979*a*, *b*; Hinkle, Hall, and Ridgway 1982, hereafter HHR; Hinkle, Scharlach, and Hall 1984, hereafter HSH). Since the atmospheric opacity of Mira variables is much less in the infrared than in the visual, infrared absorption lines sample the deep layers where the indication of shock waves is unambiguous, in contrast with shorter wavelengths (Wallerstein 1977). The best observational data presently available for sampling the deep atmospheric layers come from the 1.6 μm $\Delta v = 3$ vibration-rotation bands of CO. From spectra of these bands, HHR deduced radial velocities, excitation temperatures, and column densities at a variety of visual phases for the Mira variable χ Cyg. HSH measured the same quantities for eight additional Mira variables plus X Oph, a low-amplitude, long-period variable. In this section we analyze the observational data of HHR and HSH for the four Mira variables with the most data: *o* Cet, T Cep, χ Cyg, and R Cas. For each star the data are fitted by a spherical periodic shock model. The model fits allow us to infer the deep atmospheric structure of these Miras, from which we can estimate shock luminosities and pulsation constants.

Table 1 summarizes for each star the model input parameters: period, center-of-mass radial velocity (heliocentric), visual phase when the shock passes through the CO $\Delta v = 3$ line-forming region, postshock cooling temperature, and CO column density (in cm^{-2}). The phase offset $\Delta\phi$ is defined as the visual phase when the shock emerges through the CO $\Delta v = 3$ line-forming layer, and is estimated as the phase when the excitation temperature is a maximum. Since CO is dissociated in the strong ($\gtrsim$30 km s^{-1}) shocks present in the deep layers, the values of $\Delta\phi$ are somewhat uncertain, but probably not by enough to change the model fits appreciably. The cooling temperatures T_c are determined by a fit to the temperature variation over an entire cycle, and so may not agree precisely with the peak observed temperatures. Similarly, the stellar radial velocities v_* are determined by a model fit to the observed velocity variation, and disagree slightly with radial velocities determined from circumstellar thermally excited microwave emission lines (HSH).

The spherical periodic shock model used here has three dimensionless parameters that are determined by fitting to the data (eq. [3.14]). Of these, γ and κ depend on thermodynamics and vary in an unknown way with radius; λ depends on the shock velocity, whose dependence on radius is fixed by the model once γ and κ are given. We assume that the gas is primarily H_2, with $\mu = 2m_H$, but the results are not sensitive to this assumption. The ratios κ and λ depend on the stellar mass M, which is poorly known for long-period variables. A mass of 0.7–1.8 $M_\odot$ has been estimated for the variable component of the binary *o* Cet (Fernie and Brooker 1961). In the following we set $M = 1\ M_\odot$, but the value adopted does not affect our model fits. All of the derived parameters depending on M will be given with the explicit mass dependence.

TABLE 1

SHOCK MODEL INPUT PARAMETERS

Star	P (days)	v_* (km s^{-1})	$\Delta\phi$	T_c (K)	$\log_{10} N$(CO)
o Cet	332	58.8	−0.04	4790	23.6
T Cep	388	−17.0	−0.22	3850	24.0
χ Cyg	407	−7.0	−0.10	3960	24.3
R Cas	431	19.4	−0.04	4170	23.7

The procedure for fitting a model to the data consists of computing the velocity and temperature of a fixed (Lagrangian) fluid element as functions of phase, and then comparing them with observational data. Since the CO $\Delta v = 3$ lines have roughly constant column density over most of a period (HSH), we assume that the lines sample the same layer at a variety of phases. While this assumption is correct for a plane-parallel atmosphere, when spherical effects are properly included the column density measured to a fixed mass shell decreases when the shell rises, and increases when it falls. Because the density gradient is steep ($|d \ln \rho/d \ln r| \gg 1$), however, the resulting column-density changes (a factor of 2 or so between the minimum and the maximum radius of a fixed shell) correspond to much smaller errors in radius, velocity, and temperature. For simplicity we thus neglect the column-density variations and fit the observations as if they sample a fixed mass shell, although we will note the resulting errors.

The Lagrangian assumption clearly fails when the shock passes through the layer, because the CO is then dissociated; the column densities are observed to be smaller during these phases. The model fits are thus weighted toward intermediate phase, when the Lagrangian hypothesis seems justified. We note that the lines are doubled around the time of shock passage. This is due to absorption occurring both above and below the shock, with different velocities for these layers. To resolve the ambiguity, we set zero phase by the peak excitation temperature, for which the lines also have approximately the maximum blueshift. For doubled lines the blue component (postshock gas) is assigned the smaller possible phase (typically $0 \lesssim \phi \lesssim 0.1$), while the phase is greater by 1 ($1.0 \lesssim \phi \lesssim 1.1$) for the red component (infalling gas). The model fits are applied only for $0 \leq \phi \leq 1$, hence low column density red components of double lines are excluded.

a) Temperature

Figures 9*a*–9*d* superpose model fits and observed CO $\Delta v = 3$ excitation temperatures for the four stars analyzed. As noted by HHR, at the depths where the lines are formed it is valid to equate the excitation and kinetic temperatures. The phases are offset by an amount $\Delta\phi$ (Table 1) from phases determined by the visual light curves. Error bars were taken from HSH where available; otherwise we set errors of $\pm$200 K except for R Cas, where two points have been assigned errors of $\pm$400 K. (The error bars are shown only to aid in the graphical comparison of the model fits with the data.) The dimensionless parameters γ, κ, and λ were varied until reasonable fits by eye were obtained. Least-squares fitting was not used because there are some systematic differences between the models and the data (These differences occur primarily near the time of shock passage, when the data are not expected to sample a single layer.) We estimate model uncertainties to be $\pm$0.01 in γ and $\pm$5% in κM and λM. The temperature profiles alone determine κ well, but they fix γ and λ less well, since an increase in one of these can be nearly compensated for by a decrease in the other. Fortunately, the velocity fits are sensitive to λ but not to γ, so the ambiguity is resolved.

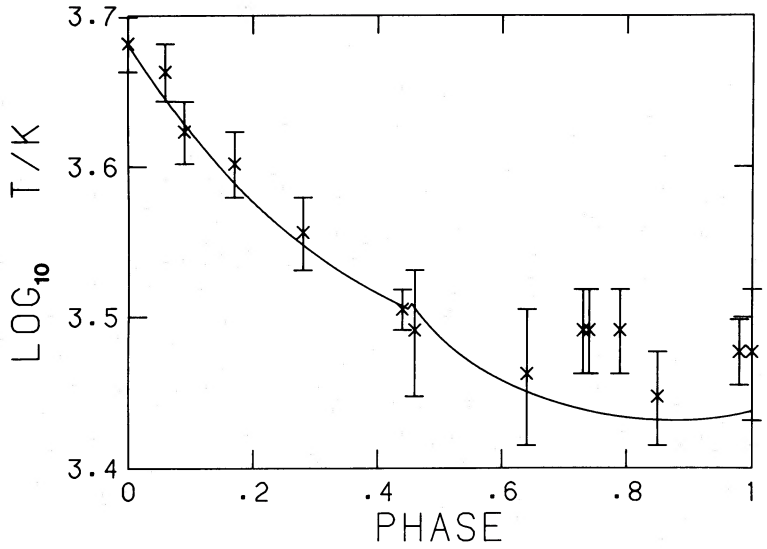

FIG. 9*a*

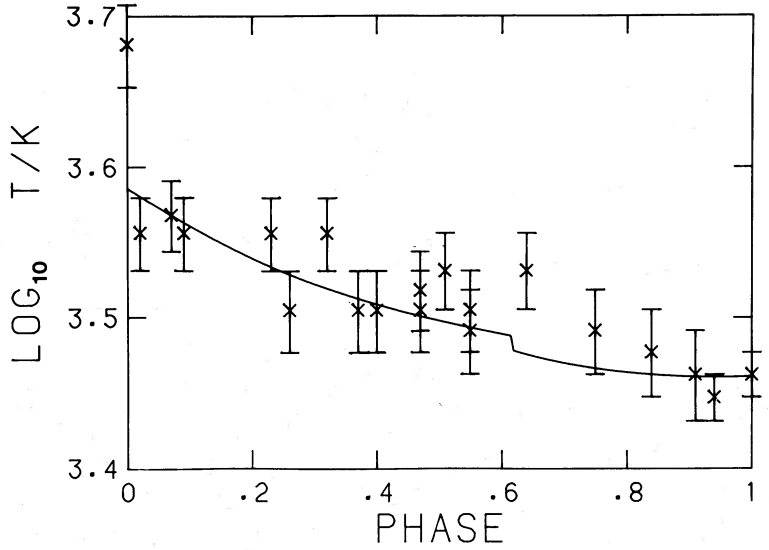

FIG. 9*b*

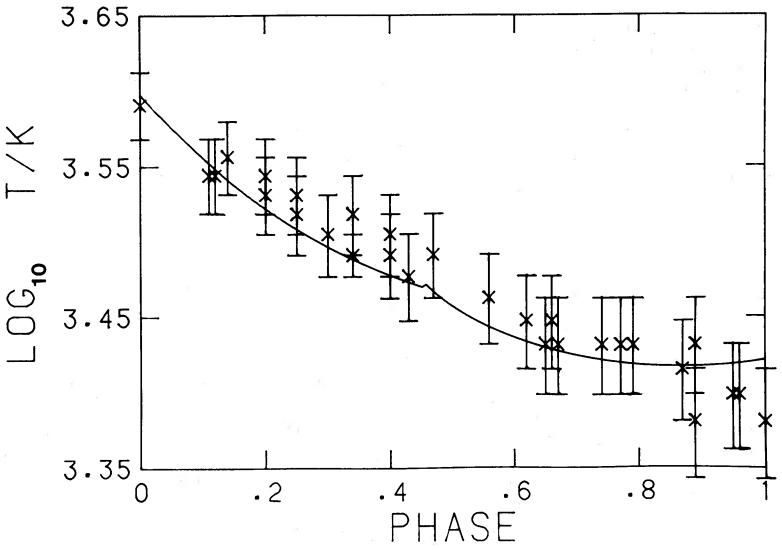

FIG. 9*c*

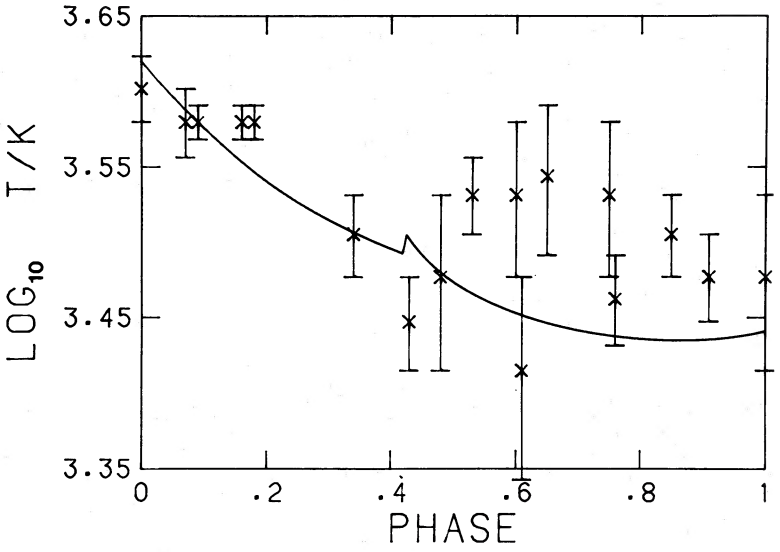

FIG. 9*d*

FIG. 9.—Observed CO $\Delta v = 3$ excitation temperatures (data points) and spherical periodic shock wave model fits (*solid curves*) for (*a*) *o* Cet, (*b*) T Cep, (*c*) χ Cyg, and (*d*) R Cas. The phase is offset from the visual phase by $\Delta\phi$. Parameters of the fits are given in Tables 1 and 2.

The glitches present at middle phases in the model temperature curves of Figure 9 are due to the switch from the plane-parallel approximation (which includes pressure forces) at early phase to the spherical ballistic approximation (which includes spherical effects but neglects pressure forces) at late phase. Since the temperature in the ballistic portion is determined by adiabaticity with the value at $\phi = 1$ set by shock jump conditions, the models do not force continuity at the break. Since the resulting discontinuities are small compared with the uncertainties in the data, we do not consider them a serious problem. An exact solution of the Lagrangian equations of motion (3.6)–(3.8) would give a smooth curve matching the approximate solution at early and late phases.

Table 2 lists the dimensionless parameters describing the shock model fit. The adiabatic exponents γ are all close to unity. The values of κ are small, showing that pressure forces are not very important except immediately postshock, as also demonstrated by the moderately large Mach numbers $\mathscr{M}_1$. The relatively large values of β (the ratio of shock to escape velocity, both measured in the stellar rest frame) indicate that the vertical amplitude of the observed layer is large. From the fits we estimate the uncertainties in $\mathscr{M}_1$ and β to be $\pm 5\%$. The last column of Table 2 gives $w_{\max}$, a dimensionless parameter reflecting the soundness of the plane-parallel and ballistic approximation used to solve the equations of motion. The approximation is valid when $w_{\max} \gg 1$. Although this condition is not strongly satisfied here, the relatively small model temperature discontinuities in Figure 9 show that in practice the approximation is satisfactory.

The model fits of Figure 9 look quite good, except for the high temperature observed in T Cep at $\phi = 0$ (visual phase -0.22) and the large scatter and high temperatures in o Cet and R Cas at late phases. HSH suggested that in R Cas the CO lines may be blended with strong H_2O lines, giving misleading results. Other possible reasons for the deviations from the model are that γ may vary somewhat even for a fixed fluid element, and that the same fluid element may not always be sampled. As noted previously, for spherical motions, constant column density implies varying fluid element. For χ Cyg the effect is to decrease the maximum radius of the sampled layer (at $\phi = 0.5$) by about 18%, increasing the temperature by about 20%. Taking account of this would make the theoretical temperature profiles slightly shallower at early phases and steeper at late phases, improving the fits.

The most important point to be gleaned from Figure 9 is that the temperature of a fixed fluid element decreases almost monotonically after it is shocked. Isothermal ($\gamma = 1$) models cannot reproduce this fact, which is a strong argument that $\gamma = d \ln p/d \ln \rho > 1$. Even the isothermal model of Wood (1979), where the temperature decreases with radius (the gas is assumed to be in local thermodynamic equilibrium with the radiation field, whose intensity diminishes with radius), would fail here because it predicts a U-shaped temperature profile, with the preshock and postshock gas having the same temperature. Since we derive adiabatic exponents that are close to unity, it is likely that radiative transfer does affect the gas thermodynamics, but fortunately in a way that can still be approximated by an adiabat along a fluid trajectory. Of course, this is not proof that the same exponent and cooling temperature apply at all radii. Most likely the cooling temperature decreases with Lagrangian radius (§ IV*d*), but this has no effect on our model fits here, since they are applied only to a fixed fluid element. Testing the thermodynamic parameters at different layers requires temperature measurements probing different depths.

TABLE 2

DERIVED DIMENSIONLESS PARAMETERS FOR CO $\Delta v = 3$ LINE-FORMING REGION[a]

Star	γ	$\kappa M \mu^{3/2}$	$\lambda M f^{-3}$	$\mathscr{M}_1 \mu^{-1/2} f^{-1}$	β	$w_{\max}$
o Cet	1.14	0.019	0.507	9.17	0.391	2.61
T Cep	1.08	0.016	0.217	6.67	0.324	2.90
χ Cyg	1.10	0.0175	0.503	8.92	0.389	2.64
R Cas	1.10	0.020	0.636	9.21	0.408	2.52

[a] M is the stellar mass in $M_\odot$, $2\mu m_H$ is the mean molecular weight of the gas, and f is a geometrical correction factor due to limb darkening which multiplies the observed radial velocities.

b) *Velocity*

Figures 10*a*–10*d* show observed velocities (measured in the stellar rest frame) and theoretical model fits for the CO $\Delta v = 3$ absorption lines. The observational errors are smaller than the symbols plotted, although the scatter present in pairs of measurements made at the same phase (separated by a whole number of periods) suggests that the true uncertainties are larger. The possibility of a geometrical or limb- darkening correction factor multiplying the observed radial velocities is included in our analysis. Parsons (1972) suggested that the observed velocity variations in Cepheids should be increased by a factor $f \approx 1.31$ to account for these effects, and similar arguments are often made for Mira variables. If the absorption occurs in a shell high above the continuum-forming region, however, $f = 1$. We found that, aside from o Cet, the velocity and temperature measurements could not both be fitted unless $fM^{-1/3} \approx 1$. In o Cet the high-velocity tail present at late phases would fit the model slightly better if $fM^{-1/3} \approx 1.2$. This suggests that if $f = 1$ for all of the variables, then o Cet has a smaller mass than the others. Note that if M is changed for fixed λ, the temperature fits will be nearly invariant provided that $\kappa M =$ constant. This is because, for large Mach number, κ just scales with the temperature.

The stellar velocities v_* listed in Table 1 were obtained from the velocity fits of Figure 10; changing v_* would shift the data points up or down. Stellar velocities have been measured for o Cet, χ Cyg, and R Cas from microwave thermal and maser emission lines (for references see HHR and HSH), and are 2–3 km s^{-1} less (i.e., bluer) than those obtained here. The reason for this discrepancy is unclear. We note that if the geometrical correction factor f varies systematically with phase, this would affect our determinations of v_* and λ. In any case the observed velocities are fairly sensitive to radiative transfer effects that previously could not be evaluated well. Evidence for such effects exists in o Cet at late phases and T Cep at early phases.

In T Cep the premaximum "hook" present in the velocity data corresponds to CO column densities that are less by factors of $\gtrsim 2$ than the other points. This difference in column densities suggests that the premaximum measurements are sampling material approximately one density scale height higher in the atmosphere. At these phases this material would be falling toward the shock, leading to bluer velocities than expected, as is observed. It is not clear why this effect should be so prominent only in T Cep; χ Cyg shows similar changes in column density near maximum (although of shorter duration) but lacks an obvious velocity hook.

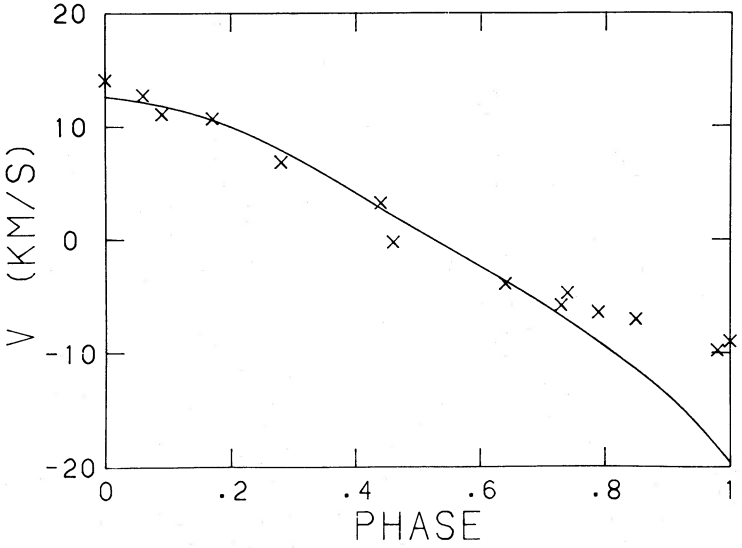

FIG. 10*a*

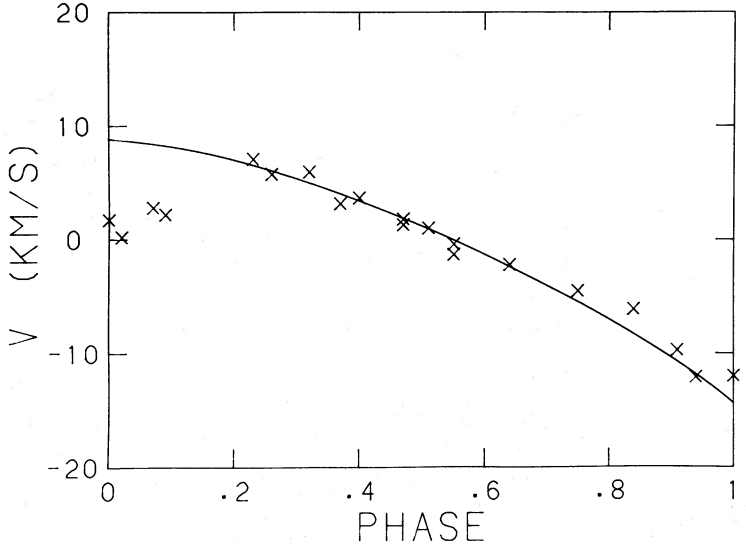

FIG. 10*b*

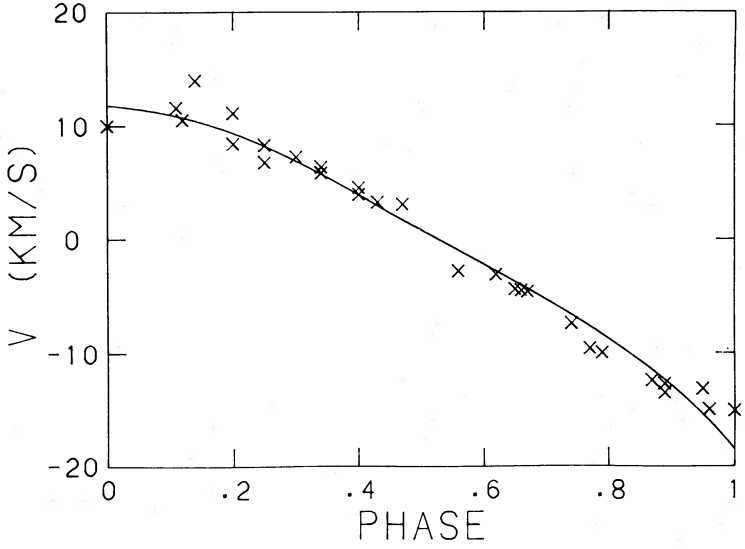

FIG. 10*c*

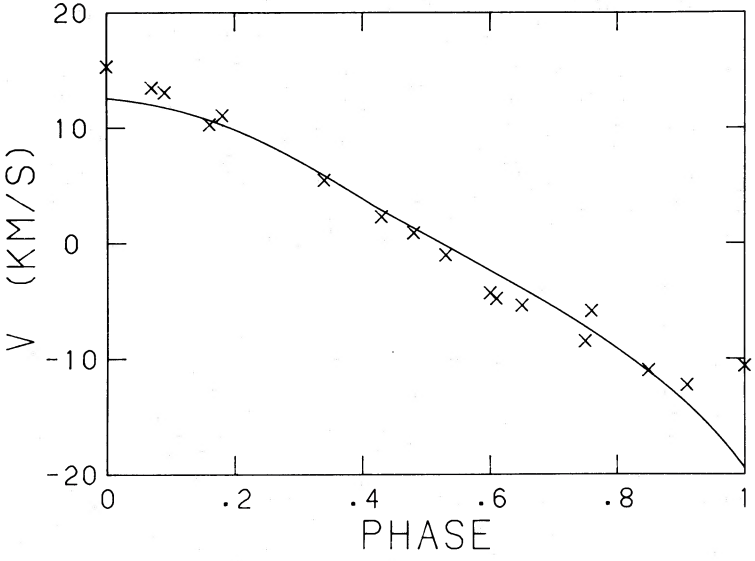

FIG. 10*d*

FIG. 10.—Observed CO $\Delta v = 3$ velocities (data points, measured in the stellar rest frame) and spherical periodic shock wave model fits (*solid curves*) for (*a*) *o* Cet, (*b*) T Cep, (*c*) χ Cyg, and (*d*) R Cas. Observational errors are smaller than the symbols plotted. The phase is offset from the visual phase by $\Delta\phi$. Parameters of the fits are given in Tables 1 and 2.

TABLE 3

DERIVED PHYSICAL PARAMETERS FOR CO $\Delta v = 3$ LINE-FORMING REGION

Star	$r_0 M^{-1} f^2$ (10^{13} cm)	$u_1 f^{-1}$ (km s^{-1})	$\rho_1 M f^{-2}$ (g cm^{-3})	QMf^{-3} (days)
o Cet	2.30	32.9	2.07×10^{-10}	0.0553
T Cep	3.08	24.0	4.22	0.0417
χ Cyg	2.62	30.9	4.51	0.0557
R Cas	2.56	32.6	2.17	0.0611

The theoretical velocity curves of Figure 10 show that the velocity of a fixed fluid element varies slowly at early phases, while the element decelerates nearly uniformly at intermediate phases, and with increasing deceleration at late phases. This behavior is easy to understand. At early phases, shortly after the element is shocked, upward-directed gas pressure forces are important, and they keep the element moving nearly at the shock velocity (cf. Figs. 2–4). At late phases pressure forces are unimportant, so the fluid element moves ballistically with acceleration $dv/dt = -g$, $g = GM/r^2$. The maximum deceleration occurs just before the element is shocked, when r is a minimum. Between phases 0.3 and 0.7 the element is higher up, so g is less than at $\phi = 0$; g changes slowly then because v is small, and thus r changes relatively little. This qualitative behavior must occur whenever there are no other forces (e.g., radiation pressure) acting on the gas. Of course, this assumes a fixed mass shell. The theoretical velocities are not corrected for mass shell variations occurring for constant column densities. These corrections increase the velocity by ~ 5 km s^{-1} at $\phi = 0$ and $\phi = 1$, compared with $\phi = 0.5$, improving the fits somewhat.

The increasing gravitational deceleration with phase can lead to faulty mass estimates for Mira variables. HHR noted that the mean deceleration is ~ 0.098 cm s^{-2} for χ Cyg, and with an estimated photospheric radius of 1.7×10^{13} cm they deduced $M \approx 0.2\ M_\odot$. But the deceleration deduced here is twice as large when the CO $\Delta v = 3$ line-forming layer is shocked. Also, the photosphere probably lies interior to this region. Both corrections increase the estimated mass; $M \approx 1\ M_\odot$ seems plausible.

An attempt was made to fit observations of the low-amplitude, long-period variable X Oph to a periodic shock model, with little success. The problem is that the velocity curve shows deceleration for only about half the period (HSH). There appears to be a premaximum "hook" as in T Cep, but is much more pronounced in X Oph. If this is due to radiative transfer effects that can be accounted for, then perhaps a satisfactory shock model fit could be obtained.

c) *Derived Parameters*

Table 3 lists for each star physical parameters derived from model fits for the CO $\Delta v = 3$ line-forming region. Columns (2)–(4) give the radius when the shock passes through this layer, the preshock velocity, and the preshock density. The dependence on the velocity correction factor f, the mean molecular weight μ, and the unknown stellar mass M stems from equations (3.9), (3.14), and (3.15). We estimate the uncertainties in r_0 and u_1 to be $\pm 5\%$; ρ_1 has larger uncertainty, as we discuss below. Column (5) gives the pulsation contant Q, defined by

$$Q \equiv P\left(\frac{\bar{\rho}}{\bar{\rho}_\odot}\right)^{1/2} = P\left(\frac{M}{M_\odot}\right)^{1/2}\left(\frac{r}{R_\odot}\right)^{-3/2}. \tag{4.1}$$

In § V*a* we discuss the implications of these pulsation constants for the mode of pulsation of Mira variables.

The density at the CO $\Delta v = 3$ line-forming layer is inferred from column-density measurements by simply integrating over radius the Eulerian density computed from model fits. Since the density above a shock (at fixed time) decreases essentially exponentially with height for a decade or so (cf. Figs. 11–13), we may write

$$\rho_1(r_0) \approx -m_{\rm H} N({\rm H})\left(\frac{\partial \ln \rho}{\partial r}\right)_{r = r_0^+}, \tag{4.2}$$

where N(H) is the column density of hydrogen nuclei in atomic or molecular form. Table 1 gives N(CO); we assume $N({\rm H})/N({\rm CO}) = 10^{3.3}$ for o Cet, T Cep, and R Cas, and $N({\rm H})/N({\rm CO}) = 10^{3.0}$ for the S-type Mira χ Cyg. These abundance ratios are somewhat uncertain, but are not as uncertain as the observed column densities, which were determined by fitting observed curves of growth to a plane-parallel isothermal model. The inferred densities may therefore be uncertain by a factor of 10 (HSH). Theoretical curves of growth based on the model atmospheres obtained here should improve the density estimates. In any case these density estimates show that the atmospheric mass is only a small part of the total stellar mass. For χ Cyg, the mass of gas lying above the CO $\Delta v = 3$ line-forming region is

$$M_{\rm atm} \approx 0.025 M^2\ M_\odot, \tag{4.3}$$

where M is the stellar mass in $M_\odot$. Thus our assumption of constant mass used in deriving the gravitational force for the models in §§ II and III is fully justified.

The model derivations also assumed that particle orbits are purely periodic, i.e., that a shocked fluid element returns after one period to exactly the same radius and velocity. Now we can show that this condition is well satisfied at the CO $\Delta v = 3$ line-forming layer. Suppose that the orbits are not closed, so that after one period a particle is shocked ar $r_0 + \Delta r$, $\Delta r > 0$. This corresponds to an outward mass flux of $\rho_1 \Delta r/P$, or a steady mass loss rate of

$$\dot{M} = \frac{4\pi r_0^2 \Delta r \rho_1}{P}. \tag{4.4}$$

For χ Cyg this gives $\Delta r/r = 22 M^{-2} \dot{M}$, where $\dot{M}$ has units of $M_\odot$ yr^{-1}. Since Mira variables typically have $\dot{M} \sim 10^{-6}\ M_\odot$ yr^{-1} (Gehrz and Woolf 1971; Bowers and Kerr 1977; Knapp and Morris 1984), $\Delta r/r \sim 2 \times 10^{-5} \ll 1$ and orbits are closed to a high degree of accuracy. Note that since ρ_1 falls rapidly (roughly exponentially) with radius, the purely periodic assumption must break down at some radius. But the density scale height is much less than r, so the periodic assumption will be good out to radii just short of the point where orbits open up and mass loss originates.

The determination of the density and temperature along a streamline allows a discussion of the thermodynamic properties of the gas. We consider χ Cyg, in which $T = 3960$ K, $\rho = 2.7 \times 10^{-8}$ g cm^{-3} at phase 0 (at the end of the shock wave cooling zone) and $T = 2500$ K, $\rho = 4.5 \times 10^{-10}$ g cm^{-3} at phase 1. Under these conditions the time scale to achieve chemical equilibrium is less than the adiabatic expansion time (Tsuji 1964), so that equilibrium molecular concentrations are applicable. We find that the fraction of H atoms in molecular form varies from about 0.5% at phase 0 to about 10% at phase 1 (Vardya 1960; Tsuji 1964). Essentially all of the C is in the

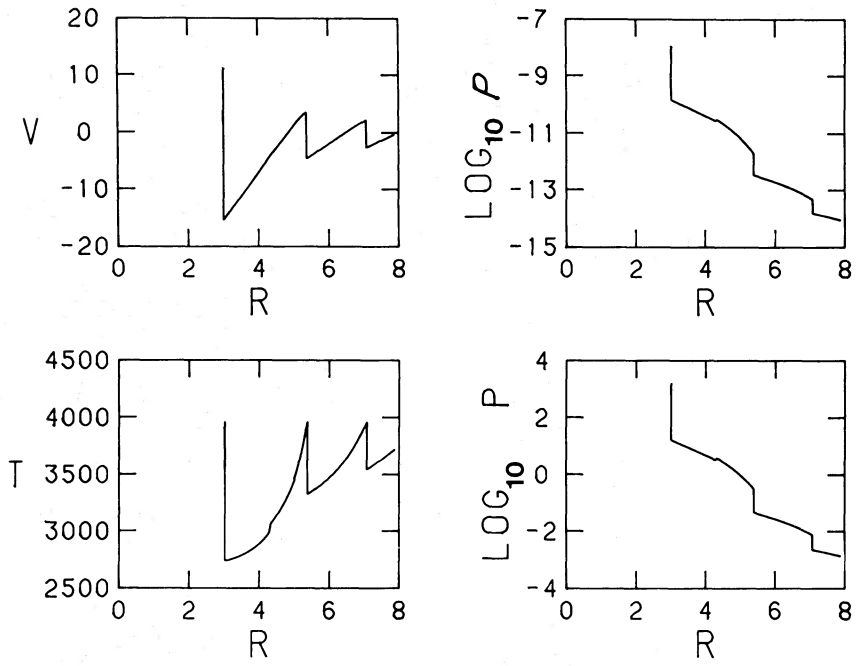

FIG. 11.—Eulerian fluid distribution at visual phase 0.0 for the spherical periodic shock wave model, with parameters set at the CO $\Delta v = 3$ line-forming layer (the innermost shell plotted) by a fit to χ Cyg. The units are 10^{13} M cm (R; M is the unknown stellar mass in $M_\odot$), km s^{-1} (V; no geometrical correction factor has been applied), M^{-1} g cm^{-3} (ρ), K (T), and $(\mu M)^{-1}$ dyn cm^{-2} (P; $2m_H\mu$ is the mean molecular weight). The extrapolation to larger radius assumes constant ratio of specific heats and cooling temperature. These assumptions lead to unrealistically high temperatures at large radii.

form of CO over the entire range of phase. This shows that the constancy of N(CO) with phase implies the constancy of total mass column density, as was assumed above.

If radiative processes are not important, the effective γ of the gas is determined by the thermodynamic equilibrium of the gas, composed primarily of hydrogen. For a gas of molecular hydrogen with vibrational degrees of freedom not excited, $\gamma = 1.4$; for molecular hydrogen with vibrations excited, $\gamma = 9/7$; and for atomic hydrogen, $\gamma = 5/3$ (e.g., Zel'dovich and Raizer 1966). In the temperature range where molecular vibrations are excited (several thousand K), molecular dissociation is usually important and can lower the effective γ of the gas. Vardya (1960) has computed adiabats for a temperature and density range which covers the conditions along the streamline in χ Cyg. At phase 0, when the gas is primarily atomic hydrogen, $\gamma_{\rm eff} \approx 1.6$, and at phase 1, when the amount of molecular

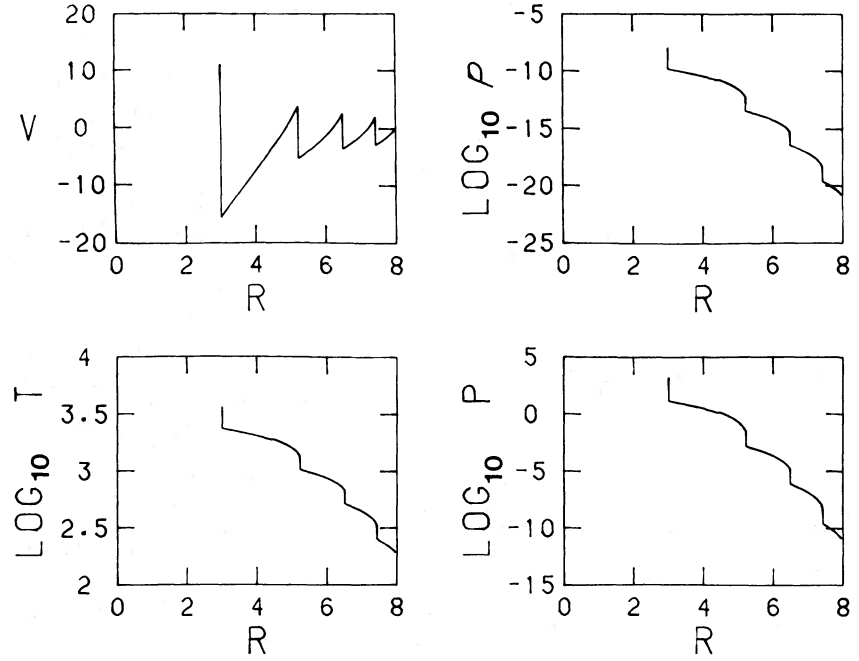

FIG. 12.—Same as Fig. 11, except that the cooling temperature is taken to decrease with radius so that the atmosphere is isentropic, i.e., $T\rho^{-(\gamma-1)}$ = constant

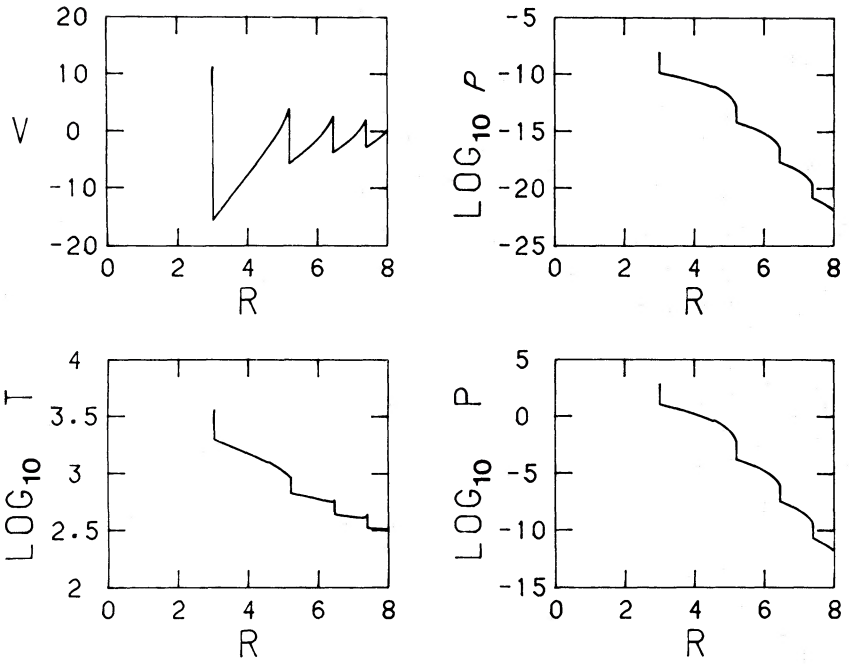

FIG. 13*a*

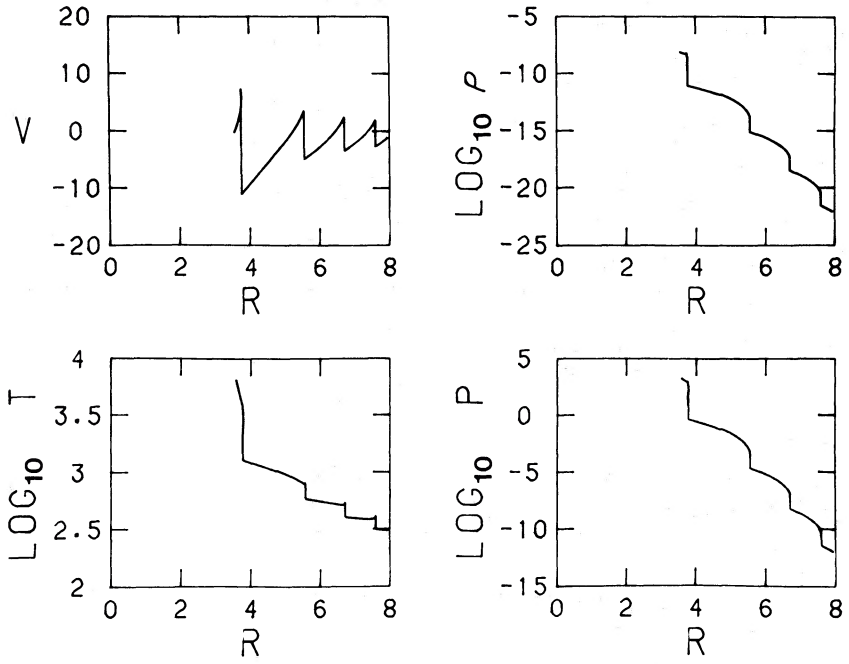

FIG. 13*b*

FIG. 13.—Eulerian fluid distributions at visual phases (*a*) 0.0, (*b*) 0.25, (*c*) 0.5, and (*d*) 0.75, computed with the assumption that the preshock temperature decreases as r^{-2}. Units and other parameters are the same as in Figs. 11 and 12. The innermost shell is taken to be at the estimated photosphere, and is shocked at visual phase −0.27.

hydrogen becomes substantial, $\gamma_{\rm eff} \approx 1.18$. The value of $\gamma_{\rm eff}$ deduced from the model fit to the observations is lower than this range, implying that radiative processes are significant. A detailed discussion of these processes lies beyond the scope of this paper.

Mira variables have long been known to have very extended atmospheres, but the strong dependence of opacity on wavelength has made observational estimates ambiguous (e.g., Labeyrie *et al.* 1977), and theoretical models have also given conflicting results (e.g., Willson 1976; Wood 1979; Hill and Willson 1979). HHR estimated the photospheric radius of χ Cyg to be 1.7×10^{13} cm, less than the radius we have derived for the CO $\Delta v = 3$ line-forming layer for $M > 0.65\ M_{\odot}$. Weak CO emission at visual phases as early as −0.3 suggests that the photosphere lies interior to the layer where the absorption lines are formed. We will further discuss the location of the

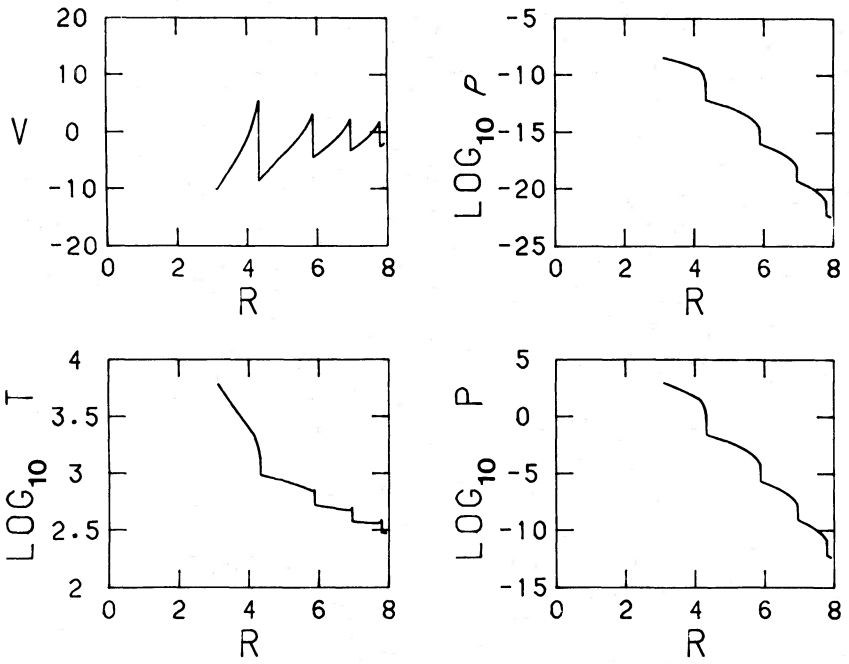

FIG. 13c

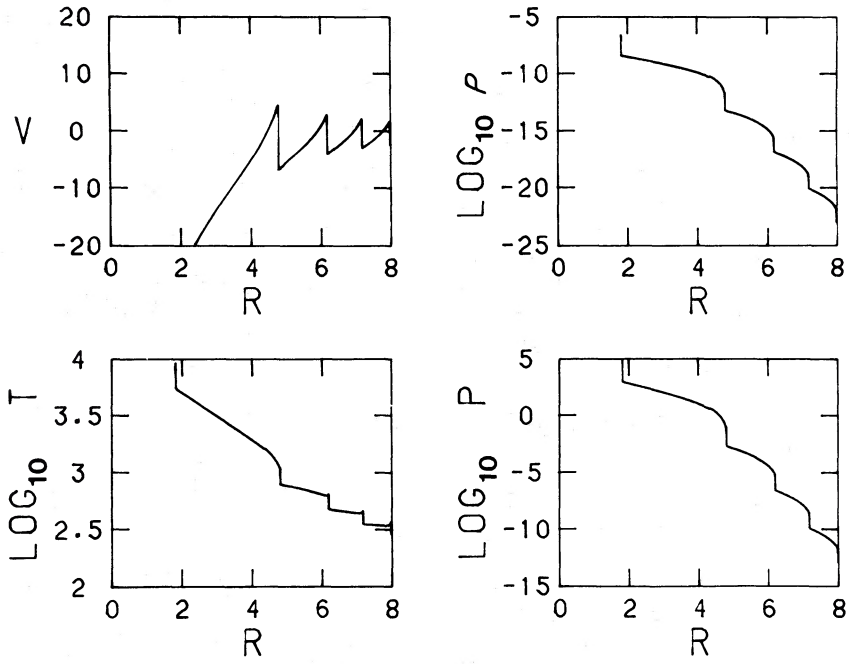

FIG. 13d

photosphere below, when we extrapolate the shock propagation to earlier and later phases.

d) Radial Structure of Mira Atmospheres

The model fits of Figures 9 and 10 and the corresponding parameters of Tables 2 and 3 apply only to a fixed Lagrangian mass shell, the CO $\Delta v = 3$ line-forming layer. But the shock models may be computed over any range in radius. While high-quality data are not yet available to test models at other depths, it is clearly desirable to extrapolate the models to make predictions. This extrapolation depends on how the thermodynamics is treated. The solution presented in Figures 5–8 assumed that the adiabatic exponent γ and cooling sound speed C_c are independent of height, but the solution method outlined in § III is more general and allows these quantities to vary with radius. Here we will present the structure of model atmospheres computed with the parameters of χ Cyg (fixed at the CO $\Delta v = 3$ layer) for the cases (1) T_c = constant, (2) $T_c \rho_c^{-(\gamma-1)}$ = constant, and (3) $T_1 \propto r^{-2}$. (T_c and ρ_c are the cooling temperature and density, and T_1 is the preshock temperature.) In all cases a constant adiabatic exponent $\gamma = 1.10$ is adopted independent of radius. Thus, the motion of

a fixed fluid element is treated as adiabatic with exponent γ, but the variation of specific entropy from element to element differs in each of the three cases considered. We emphasize that these dependences of γ and T_c on radius are only guesses and that observations at other radii are needed to pin them down. But we believe that useful insights into the atmospheric structure of Mira variables can still be obtained by extrapolating the solutions in this way.

Figure 11 shows the Eulerian fluid distribution computed for χ Cyg at visual phase 0.0 (after the shock emerges through the CO $\Delta v = 3$ line-forming layer at visual phase -0.10) for the constant cooling temperature case, corresponding to Figures 5–8. The minimum radius has been set by the CO $\Delta v = 3$ layer. The maximum radius is limited because beyond $\sim 10^{14}$ cm the shocks become too weak ($\mathcal{M}_1 \rightarrow 1$) to support a purely periodic flow. The small glitches in ρ, T, and p are due to the approximate method of solution. Three shocks are apparent, the upper two having passed through the lower layers of the star at earlier phases. As we anticipated in § II, the shock velocity and separation clearly decrease with height. The temperature remains high at large radius, however, because of the assumption T_c = constant. Because temperatures are high, the upper shocks are weak, so the density scale height increases at large radius (cf. eqs. [2.34] and [3.9]). In this model a sonic point exists around 10^{14} cm, beyond which mass loss must occur. We estimate the mass loss rate from the shock mass flux:

$$\dot{M} \sim 4\pi r_s^2 \rho_c v_s , \tag{4.5}$$

giving $\dot{M} \sim 10^{-6}\ M_\odot\ \mathrm{yr}^{-1}$ for $r_s = 10^{14}$ cm, $v_s = 4$ km s^{-1}, and $\rho_c = 1 \times 10^{-15}$ g cm^{-3} (cf. Fig. 11). We consider this coincidence with observationally inferred mass loss rates (cf. Knapp and Morris 1984) to be fortuitous, however, because the assumption of constant cooling temperature is clearly unrealistic. Gas at nearly 4000 K will cool relatively quickly because of the low opacity present high above the photosphere.

A slightly more plausible temperature distribution results from assuming that the stellar atmosphere is isentropic, i.e., $T_c \rho_c^{-(\gamma-1)}$ = constant. In this case the specific entropy (defined with respect to the index γ) of the gas is constant not only for a fixed fluid element but also for different elements. The temperature is thus everywhere given by the density: $T = K\rho^{\gamma-1}$, where K is a constant. The isentropic assumption may be reasonable if the gas does not interact with the radiation, although it is unreasonable to expect that $\gamma = 1.10$ everywhere. Figure 12 shows the resulting Eulerian structure, with the same parameters as Figure 11. Now the temperature decreases monotonically with radius, because the density does. Consequently the shocks do not weaken steadily with radius; in fact, they strengthen at large radius because the shock velocity is falling only as a power of radius but the sound speed is falling exponentially.

In spite of the very different thermodynamic properties of the model atmospheres shown in Figures 11 and 12, the velocity profiles, hence fluid and shock trajectories, are quite similar. This similarity occurs because, so long as the shocks are strong, the fluid trajectories are nearly ballistic. The velocity profiles differ significantly only where the shocks weaken in Figure 11. Thus absorption-line radial velocities measured over a period can in principle give a good estimate of the height at which the lines form, even without accurate excitation temperatures or column densities. In practice, unfortunately, this method works well only for deep layers where the velocity variation is large.

The isentropic assumption, although more reasonable in our view than the isothermal cooling (T_c = constant) assumption, neglects the interaction between the gas and radiation. We are thus led to consider the case where the gas and radiation are strongly coupled, at least at some phases. The stellar bolometric luminosity (neglecting the postshock emission) is

$$L = 4\pi r_p^2 \sigma T_e^4 , \tag{4.6}$$

where r_p is the photospheric radius and T_e is the effective temperature of the radiation field. Assuming that the shocks are well outside the photosphere (this is probably not true; see below) and that the preshock gas is optically thin and in thermal equilibrium with the radiation field, equation (4.6) generalizes to give $T_1 \propto r^{-2}$. (The postshock gas is much hotter, but we suppose that the gas can come into equilibrium with the radiation just before it is shocked again.) This condition gives the radial dependence of κ implicitly (specifying T_c gave κ explicitly from eq. [3.14]), but it is easy numerically to find $\kappa(r_s)$ and thus the radial dependence of the solution.

Figures 13*a*–13*d* show the Eulerian structure computed for χ Cyg with $T_1 \propto r^{-2}$ at visual phases 0.0, 0.25, 0.5, and 0.75. The solution has been extrapolated both inward and outward from the CO $\Delta v = 3$ line-forming layer; the innermost shell is shocked at visual phase -0.27 at a radius of $1.7 \times 10^{13}\ Mf^2$ cm, chosen to correspond to the photospheric radius estimated by HSH. (A few of the inner Lagrangian shells have been omitted from Fig. 13*a*, because slight shell-crossing occurred as a result of our approximate method of solution.) The outer boundary is arbitrary in the model, but we will argue in § V*b* that the purely periodic assumption, and hence the model, breaks down at $r \approx 5 \times 10^{13}\ M$ cm. We consider the thermodynamic assumptions made here to be the most reasonable of the three cases considered. The solution is presented at several phases to show the time dependence of the atmospheric structure.

Comparison of Figures 12 and 13*a* shows that the particle orbits are virtually indistinguishable, while the temperature profiles are fairly different. As noted above, particle orbits are ballistic in the strong shock limit, which applies in both figures. In Figure 13, however, because of the slow radial decrease in temperature, the Mach number $\mathcal{M}_1$ does decrease at large radius. ($\mathcal{M}_1 = 3.3$ at $r_s = 10^{14}\ M$ cm.) Another point to note in comparing Figures 12 and 13*a* is that the thermodynamic variables (particularly the density) do not differ greatly for $r < 6 \times 10^{13}\ M$ cm. We therefore hope that real Mira atmospheres have similar profiles, allowing us to make order-of-magnitude estimates of mass loss in § V*b*.

It is interesting to compare Figure 13*a* with Figure 7 of Wood (1979), who used an Eulerian finite-difference scheme to integrate the fluid equations numerically. To drive a shock through the atmosphere, Wood applied a sinusoidally varying pressure at the inner boundary, which was fixed in radius. He assumed that the gas is isothermal, with temperature depending on radius as r^{-2} far above the photosphere, which he set at 3.1×10^{13} cm. His thermodynamic assumptions were thus similar to those adopted here, except that the temperature was not allowed to jump across a shock. Wood's numerical results agree qualitatively with those obtained here, but his velocities are about 40% smaller. Consequently his shocks are weaker and the density profile falls off less steeply than in Figure 13. Increasing the amplitude of pressure variation at the inner

boundary did not on average increase the velocities, but instead resulted in orbits bifurcating, with alternate shocks propagating with different velocities. Since observed CO $\Delta v = 3$ velocities are constant from cycle to cycle (at least for the Mira variables observed by HSH), this behavior, similar to that observed in RV Tau variables, may be a result of Wood's inner boundary condition or numerical treatment. Our solution method, since it assumes the shocks to be fully developed and enforces periodicity, does not allow study of this period-doubling phenomenon.

The time sequence of Figure 13 shows the shocks propagating up through the stellar atmosphere with advancing phase. As a shock propagates upward, it slows roughly as $v_s \propto r_s^{-1.5}$ as long as it remains strong. Figure 13 also shows the periodic motion of the inner shell, rising until visual phase 0.25, and then falling back down to be shocked at visual phase 0.73, just before the last snapshot. The velocity jump across the shock is $u_1 = 48.9$ km s^{-1} at this minimum radius. In a Mira variable the shock results from a nonlinear steepening of a general stellar pulsation, and the shock is probably not this strong when it first appears. Such a large shock velocity would partially ionize He and produce He I emission, which is not seen (G. Wallerstein 1985, private communication).

One additional observational test of the shock model, which gives good agreement with Figure 13, comes from the low-excitation CO $\Delta v = 2$ lines. For visual phases between 0.03 and 0.27, HHR measured in χ Cyg a component with excitation temperature 800 ± 100 K, column density $N(\mathrm{CO}) = 10^{22.0}$ cm^{-2}, and velocity within a few km s^{-1} of the stellar rest velocity. For the density profiles of Figures 13*a* and 13*b* the observed column density corresponds to $\rho \approx 1.0 \times 10^{-13}$ g cm^{-3} or a radius just interior to the second shock at $r = (5\text{–}6) \times 10^{13}$ M cm. Happily, the model postshock temperatures are about right, $T_c \approx 800$–900 K, suggesting that our thermodynamic assumption $T_1 \propto r^{-2}$ may not be very far off the mark. We would predict the lines to be blueshifted by 3–4 km s^{-1} more than is observed, however, although the observed lines are ~ 8 km s^{-1} across in the core. SiO maser emission (Kaifu, Buhl, and Snyder 1975; Snyder and Buhl 1975) and some visual absorption lines (Willson, Wallerstein, and Pilachowski 1982) proably originate at about this same radius (HHR), but it is difficult to prove this without column densities or excitation temperatures.

Figure 14 plots the radius of Lagrangian fluid trajectories and shock lines against time (visual phase) for the shock model of Figure 13. Trajectories are shown for every factor of 4 decrease in preshock density. Slight shell-crossing occurs for the lowest shells because of the plane-parallel and spherical ballistic approximation used, but this has no effect on the CO $\Delta v = 3$ line-forming layer. Note that the vertical amplitude is more than a factor of 2 for the lowest shells, but decreases with height as the shock velocity decreases.

Figure 15 plots on the same scale the visual light curve of χ Cyg (Campbell 1955) and the shock luminosity $L_s = 4\pi r_s^2 F_s$ (with F_s given by eq. [2.32], using the model described above) versus visual phase. The luminosity scale depends on the observed CO column densities and could be a factor of 10 too high. The visual light curve has been shifted vertically to produce the best fit between maximum and minimum. Observations show shock emission beginning in χ Cyg as early as visual phase -0.3 (HHR); we chose the innermost shell to be shocked at phase -0.27. The radius and luminosity where the shock originates are uncertain, however, because, as noted above, the shock does not begin fully developed. Our model therefore overestimates the shock luminosity and velocity at early premaximum phases. The minimum shock radius of 1.7×10^{13} M cm is thus a lower limit, and a peak shock luminosity of 10^4 $L_\odot$ (assuming no error in the column density) is probably reasonable.

The infrared light curve of Mira variables has small amplitude (1–2 mag at 2 μm; Hinkle 1978), while the visual amplitude is 8 mag for χ Cyg (HSH). We propose that the large increase in visual luminosity at early phases comes from the shock emission, and justify this by the good fit for postmaximum phases. Fox, Wood, and Dopita (1984) observed luminosities as high as 1.8 $L_\odot$ in Hγ alone for *o* Cet at visual phase -0.03. The Balmer lines show strong overlying absorption at early phases (Gillet, Maurice, and Baade 1983; Fox, Wood,

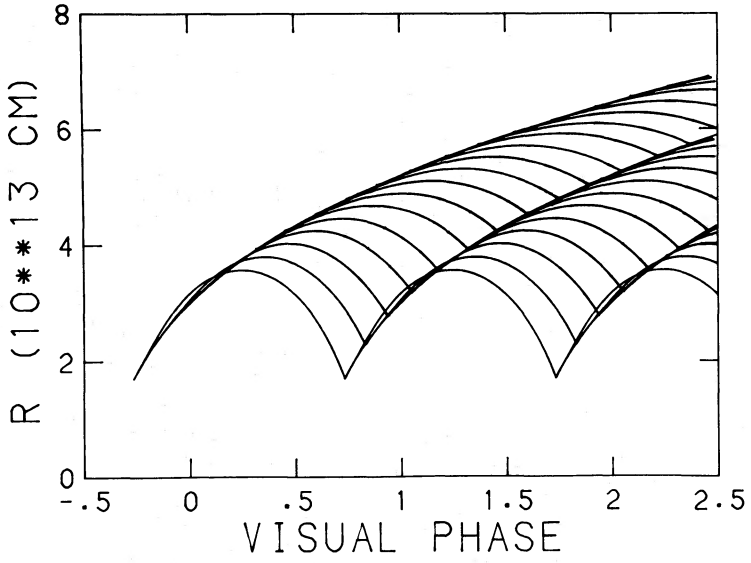

FIG. 14.—Spacetime diagram for the model atmosphere of Fig. 13. The monotonic curves are shock lines, while the oscillating curves give fluid trajectories for every factor of 4 decrease in preshock density. The approximate method of solution leads to slight shell-crossing in the densest layers.

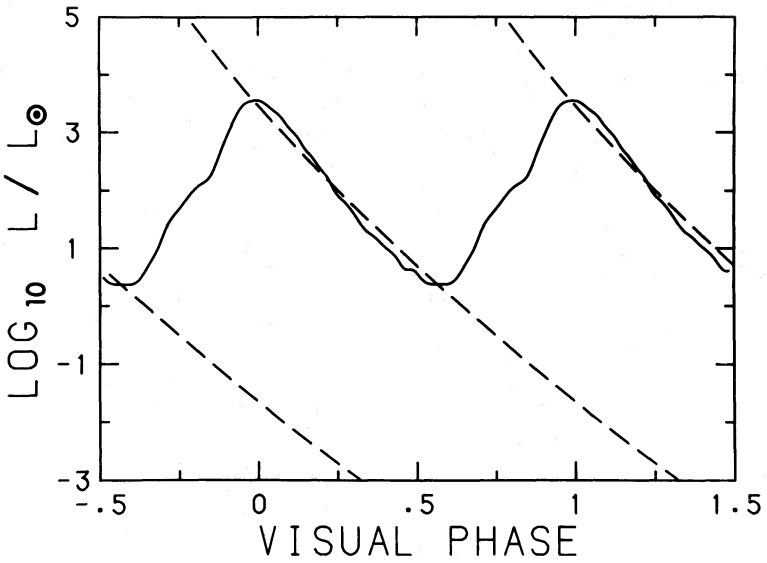

FIG. 15.—Visual light curve (*solid curve*, shifted vertically to fit model) and shock luminosity (*dashed curves*) for the model atmosphere of Fig. 13, versus visual phase. Uncertainties in measured column densities make the luminosity scale uncertain by a factor of 10. The model overestimates L_s at phases $\ll -0.10$ by assuming the shock to be fully developed. The good fit for phases between 0.0 and 0.6 suggests that over most of the cycle the visual luminosity comes from downgraded shock emission.

and Dopita 1984), so the emitted line luminosities are undoubtedly much larger. Most of the photons emitted behind the shock are absorbed and scattered many times before escaping, so rather than coming out entirely in lines, the shock radiation is spread over the entire visible spectrum. Spectrophotometry (from 4000 Å to the blackbody peak near 2μ) should provide a test of this hypothesis.

Figure 15 shows that the shock luminosity decreases rapidly with phase, even if the shock remains radiative. By visual phase 0.5, L_s is only 10^{-3} of the value at visual maximum. We suggest that the disappearance of the emission lines at intermediate phase (Gillet, Maurice, and Baade 1983; Fox, Wood, and Dopita 1984) is due to this steep decrease in shock luminosity, rather than the shock becoming too weak to excite hydrogen collisionally (Wood 1979). Note also that after one period the shock luminosity is down by a factor of 10^{-6}. We are therefore skeptical of claims (Gillet, Maurice, and Baade 1983) that emission has been seen from two shocks at the same phase.

V. DISCUSSION

The periodic shock model derived in §§ II and III shows good agreement with detailed observations (§ IV). With this success we are encouraged to test whether the model can resolve two key debates concerning Mira variables, viz., the pulsation mode and the origin of mass loss. The results are encouraging but not definitive, as we show below (§§ V*a*, V*b*). More observations are needed, and in § V*c* we suggest several fruitful areas for both observational and theoretical work.

a) Pulsation Mode

Considerable debate exists regarding whether Mira variables pulsate in the fundamental (Hill and Willson 1979) or the first-overtone (Wood 1974, 1979) mode. The primary observational test is the pulsation constant Q (eq. [4.1]). Theoretical stellar models (Keeley 1970; Wood 1974; Fox and Wood 1982) show that fundamental-mode pulsators have $Q \gtrsim 0.09$ days, while first-overtone pulsation gives $Q \lesssim 0.06$ days. Table 3 lists the pulsation constants obtained by model fits to the CO $\Delta v = 3$ line-forming layer. For $Mf^{-3} \approx 1\ M_\odot$, the results are somewhat ambiguous, with $Q \approx 0.06 M^{-1} f^3$ days aside from T Cep, which has an unusual velocity curve. However, we noted in § IV*d* that the shocks originate at a smaller radius, perhaps in or near the photosphere. In discussing the pulsation mode, Q should be evaluated at this lower height, since $Q \propto r^{-3/2}$ at larger radii. For χ Cyg we obtained a lower limit to the photosphere radius of $1.7 \times 10^{13}\ Mf^{-2}$ cm, giving

$$0.06 \text{ days} \lesssim QMf^{-3} \lesssim 0.11 \text{ days} . \quad (5.1)$$

Our best estimate of the photospheric radius of χ Cyg is $r_p \approx (1.88 \pm 0.15) \times 10^{13}\ Mf^{-2}$ cm, obtained by assuming a constant shock velocity $v_s = 12.4$ km s^{-1} interior to the CO $\Delta v = 3$ line-forming layer and assuming that the shock begins in the photosphere at visual phase -0.27. This gives

$$QMf^{-3} \approx 0.09 \pm 0.01 \text{ days} , \quad (5.2)$$

consistent with fundamental-mode pulsation for $Mf^{-3} \lesssim 1\ M_\odot$, or first-overtone pulsation for $Mf^{-3} \gtrsim 2\ M_\odot$. Unfortunately, existing mass estimates for long-period variables are inconclusive (Fernie and Brooker 1961), although the models fits presented above slightly favor $Mf^{-3} \approx 1\ M_\odot$ (fundamental mode). Accurate stellar masses and improved photospheric radius estimates (from analysis of emission lines) are necessary before the pulsation mode question can be confidently resolved.

b) Mass Loss

Deriving theoretical mass loss rates requires knowing the structure of Mira atmospheres at radii a factor of 2 or so beyond where the CO $\Delta v = 3$ lines form. Since detailed observations are not yet available to give the structure at large radii, we rely here on the extrapolated model shown in Figure 13. In support of this model we note (§ IV*d*) that it roughly fits the visual light curve and the few data points available from low-excitation CO $\Delta v = 2$ measurements of HHR, but we caution that since our model assumes no mass loss, only order-of-magnitude estimates can be obtained from it.

Observations indicate that mass loss rates of $10^{-6}\ M_\odot\ \mathrm{yr}^{-1}$ are typical for long-period variables (Knapp and Morris 1984). The most widely accepted explanation is radiation pressure acting on dust grains that form in the cool extended envelopes (Hoyle and Wickramasinghe 1962; Kwok 1975). Atmospheric shock waves have also been suggested as either the dominant mechanism (Willson and Hill 1979; Jones, Ney, and Stein 1981) or as an aid to the dust mechanism (Wood 1979). We consider here the role of shocks in mass loss in light of the atmospheric model presented in Figure 13.

Refractory materials (Si, Fe, etc.) can begin condensing to form solid grains once the gas cools to a temperature $T_{\rm con} \approx$ 1500 K (Field 1974). If the stellar radiation field is sufficiently strong, we can approximate the mass loss process by assuming that all the material lifted up to a height $r_{\rm con}$, where $T = T_{\rm con}$, is driven away. This obviously changes the atmospheric structure from that shown in Figure 13. But because the density scale height is small compared with $r_{\rm con}$, the purely periodic solution will be correct nearly out to this radius (cf. eq. [4.4]). We can thus use equation (4.5) and Figure 13 to estimate the rate at which matter is raised up by shocks to the height where grains can form, and hence the mass loss rate. From Figure 13 we estimate $r_{\rm con} \approx 5 \times 10^{13}$ cm, where the shock velocity is $v_s \approx 5$ km s^{-1}, and the density is $\rho_{\rm con} \approx 10^{-14}$ g cm^{-3}. These numbers give $\dot{M} \sim 3 \times 10^{-6}\ M_\odot\ \mathrm{yr}^{-1}$. This rate should be considered an upper limit because matter clearly cannot rise up to $r_{\rm con}$ as fast as the shock. Also note that a small uncertainty in $r_{\rm con}$ results in a large uncertainty in $\rho_{\rm con}$ (and hence $\dot{M}$), because of the nearly exponential density distribution. A proper numerical calculation, instead of the rough arguments used here, gives about the same values for $r_{\rm con}$, v_s, and $\rho_{\rm con}$ but a mass loss rate about 10 times less (Wood 1979). We conclude that grain formation in a shock-driven atmosphere can probably produce the large observed mass loss rates.

Mass loss can occur without grain formation if the shock-heated gas is unable to cool (Wood 1979; Willson and Hill 1979). In this case the specific entropy of a fluid element will increase each period, and it will be unable to return to the same height. Each additional shock kicks the particle further up, until eventually it is ejected. To estimate the mass loss rate here, we need to know how the gas cools. At temperatures below 2000 K the gas is mainly H_2, and cooling occurs by collisional excitation of molecular lines. The radiative cooling time for H_2 at a shock temperature T_2 is $t_{\rm cool} \approx n(\mathrm{H}_2)kT_2/\Lambda(T_2)$. The postshock temperature T_2 is the postshock temperature given by the Rankine-Hugoniot conditions, i.e., it is the temperature before the gas radiatively cools. The criterion for mass loss to occur is (to order of magnitude) $t_{\rm cool}/P > 1$. Setting $P \approx 1$ yr and using the high-density cooling function of Lepp and Shull (1983), this gives $T_2 \lesssim 1500$ K, the same as the dust condensation temperature. But the shock temperature is higher than the cooling temperature at the same radius, so $T_2 \approx 1500$ K corresponds to a slightly larger radius, $r_s = 5.5 \times 10^{13}$ cm, and a smaller velocity, $v_2 \approx 4$ km s^{-1}. The postshock density given by the Rankine-Hugoniot conditions is $\rho_2 \approx 4 \times 10^{-15}$ g cm^{-3}. Combining these values gives an estimated mass loss rate one-third as large as that obtained in the dust acceleration picture, or $1 \times 10^{-6}\ M_\odot\ \mathrm{yr}^{-1}$. The uncertainties in both estimates are larger than a factor of 3, however. Thus the breakdown of gas cooling can lead to mass loss as well. Even if the cooling breakdown process can produce a large enough $\dot{M}$, however, the terminal velocity could not exceed $v_s \approx 5f$ km s^{-1}, which is only half as large as observed (Zuckerman 1980). We conclude that radiative acceleration of dust grains is needed to produce the high outflow velocities, but the breakdown of radiative cooling may help to increase the mass flux.

c) *Suggestions for Further Work*

The periodic shock wave model has been applied in this paper to Mira variables, but the derivation presented in §§ II and III is quite general, requiring only the three assumptions of periodicity, radiative shocks, and adiabatic postshock motion. It is thus logical to apply the model to other pulsating variables with shocks, e.g., W Virginis stars (Wallerstein 1959) and RR Lyrae variables (Hill 1972). Atmospheric models could lead to a better understanding of the structure and evolution (through mass loss) of these stars.

The application of the shock models to Mira variables presented above could not have proved so useful without the detailed infrared absorption-line observations of HHR and HSH. Column densities were especially valuable because they showed where the CO $\Delta v = 3$ vibration-rotation lines form, and they allowed the density to be determined. Clearly it would be useful to have similar data for lines with different oscillator strengths and excitation energies, so that different atmospheric layers are sampled.

Emission-line measurements also can provide valuable information about the atmosphere. We have suggested that essentially all of the optical luminosity near maximum phase is produced by shock emission. Since most of these photons are scattered many times before escaping, visual and infrared emission-line measurements and spectrophotometry would be helpful in testing this hypothesis.

On the theoretical side, the model presented here can be improved in several ways. First, instead of using an approximate solution of the fluid equations, a more accurate numerical solution can be obtained. The novelty of our method is to treat the shocks analytically by calculating their trajectories separately and using the jump conditions explicitly, rather than using numerical or artificial viscosity. This Lagrangian technique works well because the periodicity means that we only have to compute one shock trajectory to have them all. A more accurate Lagrangian method would solve the fluid equations numerically between shocks using only a small portion of the spacetime diagram (Fig. 14) to represent the entire plane.

The shock model can also be generalized to include steady mass loss. In this case fluid orbits do not close, but there is a steady mass flux from the stellar interior replenishing the lower atmosphere, so that the Eulerian structure is unchanged after one period. This type of model would allow mass loss rates to be calculated more precisely.

With the shock model results obtained here, it is possible to go back, after the hydrodynamics has been done, to compute the radiative transfer independently. Because the atmospheric structure of Mira variables is so complicated, radiative transfer calculations are needed to compare the model with observations in all but the simplest cases.

In conclusion, we believe that the present work provides several useful tools for interpreting the detailed observations that are now becoming available for Mira variables. We hope that this work will encourage increased efforts to understand their fascinating structure and behavior.

We thank George Wallerstein and Lee Anne Willson for helpful comments and suggestions. This work was supported by NSF grants AST80-19569 and 84-13138.

REFERENCES

Bowers, P. F., and Kerr, F. J. 1977, *Astr. Ap.*, **57**, 115.
Campbell, L. 1955, *Studies of Long-Period Variables* (Cambridge: AAVSO).
Clark, F. O., Troland, T. H., Lovas, F. J., and Schwartz, P. R. 1981, *Ap. J. (Letters)*, **244**, L99.
Fernie, J. D., and Brooker, A. A. 1961, *Ap. J.*, **133**, 1088.
Field, G. B. 1974, *Ap. J.*, **187**, 453.
Fox, M. W., and Wood, P. R. 1982, *Ap. J.*, **259**, 198.
Fox, M. W., Wood, P. R., and Dopita, M. A. 1984, *Ap. J.*, **286**, 337.
Gehrz, R. D., and Woolf, N. J. 1971, *Ap. J.*, **165**, 285.
Gillet, D., and Lafon, J.-P. J. 1983, *Astr. Ap.*, **128**, 53.
———. 1984, *Astr. Ap.*, **139**, 401.
Gillet, D., Maurice, E., and Baade, D. 1983, *Astr. Ap.*, **128**, 384.
Goldreich, P., and Scoville, N. 1976, *Ap. J.*, **205**, 144.
Gorbatskii, V. G. 1961, *Soviet Astr.—AJ*, **5**, 192.
Hill, S. J. 1972, *Ap. J.*, **178**, 793.
Hill, S. J., and Willson, L. A. 1979, *Ap. J.*, **229**, 1029.
Hinkle, K. H. 1978, *Ap. J.*, **220**, 210.
Hinkle, K. H., and Barnes, T. G. 1979*a*, *Ap. J.*, **227**, 923.
———. 1979*b*, *Ap. J.*, **234**, 548.
Hinkle, K. H., Hall, D. N. B., and Ridgway, S. T. 1982, *Ap. J.*, **252**, 697 (HHR).
Hinkle, K. H., Scharlach, W. W. G., and Hall, D. N. B. 1984, *Ap. J. Suppl.*, **56**, 1 (HSH).
Hoyle, F., and Wickramasinghe, M. C. 1962, *M.N.R.A.S.*, **124**, 417.
Jones, T. W., Ney, E. P., and Stein, W. A. 1981, *Ap. J.*, **250**, 324.
Joy, A. H. 1954, *Ap. J. Suppl.*, **1**, 39.
Kaifu, N., Buhl, D., and Snyder, L. E. 1975, *Ap. J.*, **195**, 359.
Keeley, D. A. 1970, *Ap. J.*, **161**, 657.
Knapp, G. R., and Morris, M. 1984, preprint (POP-116).
Kwok, S. 1975, *Ap. J.*, **198**, 583.
Labeyrie, A., Koechlin, L., Bonneau, D., Blazit, A., and Foy, R. 1977, *Ap. J. (Letters)*, **218**, L75.
Lepp, S., and Shull, J. M. 1983, *Ap. J.*, **270**, 578.
Maehara, H. 1971, *Pub. Astr. Soc. Japan*, **23**, 503.
Merrill, P. W. 1947, *Ap. J.*, **106**, 274.
Parsons, S. B. 1972, *Ap. J.*, **174**, 57.
Reid, M. J. 1976, *Ap. J.*, **207**, 784.
Shull, J. M., and McKee, C. F. 1979, *Ap. J.*, **227**, 131.
Snyder, L. E., and Buhl, D. 1975, *Ap. J.*, **197**, 329.
Tsuji, T. 1964, *Ann. Tokyo Astr. Inst.*, **9**, 1.
———. 1971, *Pub. Astr. Soc. Japan*, **23**, 275.
Vardya, M. S. 1960, *Ap. J. Suppl.*, **4**, 281.
Wallerstein, G. 1959, *Ap. J.*, **130**, 560.
———. 1977, *J.R.A.S. Canada*, **71**, 298.
Willson, L. A. 1976, *Ap. J.*, **205**, 172.
———. 1982, in *Pulsations in Classical and Cataclysmic Variable Stars*, ed. J. P. Cox and C. J. Hansen (Boulder: Joint Institute for Laboratory Astrophysics), p. 269.
Willson, L. A., and Hill, S. J. 1979, *Ap. J.*, **228**, 854.
Willson, L. A., Wallerstein, G., and Pilachowski, C. A. 1982, *M.N.R.A.S.*, **198**, 483.
Wood, P. R. 1974, *Ap. J.*, **190**, 609.
———. 1979, *Ap. J.*, **227**, 220.
———. 1982, in *Pulsations in Classical and Cataclysmic Variable Stars*, ed. J. P. Cox and C. J. Hansen (Boulder: Joint Institute for Laboratory Astrophysics), p. 284.
Zel'dovich, Ya. B. and Raizer, Yu. P. 1966, *Physics of Shock Waves and High-Temperature Hydrodynamic Phenomena* (New York: Academic).
Zuckerman, B. 1980, *Ann. Rev. Astr. Ap.*, **18**, 263.

EDMUND BERTSCHINGER and ROGER A. CHEVALIER: Astronomy Department, University of Virginia, P.O. Box 3818, Charlottesville, VA 22903